THESIS

A POTENTIAL VORTICITY DIAGNOSIS OF TROPICAL CYCLONE TRACK FORECAST ERRORS

Submitted by

Tyler Warren Barbero

Department of Atmospheric Science

In partial fulfillment of the requirements

For the Degree of Master of Science

Colorado State University

Fort Collins, Colorado

Summer 2023

Master's Committee:

Advisor: Michael M. Bell

Elizabeth A. Barnes
Jan-Huey Chen
Philip J. Klotzbach
Yongcheng Zhou

ABSTRACT

A POTENTIAL VORTICITY DIAGNOSIS OF TROPICAL CYCLONE TRACK FORECAST ERRORS

A tropical cyclone (TC) can cause significant impacts on coastal and near-coastal communities from storm surge, flooding, intense winds, and heavy rainfall. Accurately predicting TC track is crucial to providing affected populations with time to prepare and evacuate. Over the years, advancements in observational quality and quantity, numerical models, and data assimilation techniques have led to a reduction in average track errors. However, large forecast errors still occur, highlighting the need for ongoing research into the causes of track errors in models.

We use the piecewise potential vorticity (PV) inversion diagnosis technique to investigate the sources of errors in track forecasts of four high-resolution numerical weather models during the hyperactive 2017 Atlantic hurricane season. The piecewise PV inversion technique is able to quantify the amount of steering, as well as steering errors, on TC track from individual large-scale pressure systems. Through the systematic use of the diagnostic tool, errors that occur consistently (model biases) could also be identified.

TC movement generally follows the atmospheric flow generated by large-scale environmental pressure systems, such that errors in the simulated flow cause errors in the TC track forecast. To understand how the environment steers TCs, we use the Shapiro decomposition to remove the TC PV field from the total PV field, and the environmental (i.e., perturbation) PV field is isolated. The perturbation PV field was partitioned into six systems: the Bermuda High and the Continental High, which compose the negative environmental PV, and quadrants to the northwest, northeast, southeast, and southwest of the TC, which compose the positive environmental PV. Each piecewise PV perturbation system was inverted to retrieve the balanced mass and wind fields. To quantify the steering contribution in individual systems to TC movement, a metric called the deep layer mean steering flow (DLMSF) is defined, and errors in the forecast DLMSF were calculated by comparing the forecast to the analysis steering flow. Lag correlation analyses of DLMSF errors and track errors showed moderate-high correlation at -24 to 0 hrs in time, which indicates that track errors are caused in part by DLMSF errors.

Three hurricanes (Harvey, Irma, and Maria) were analyzed in-depth and errors in their track forecasts are attributed to errors in the DLMSF. A basin-scale analysis was also performed on all hurricanes in the 2017 Atlantic hurricane season. The DLMSF mean absolute error (MAE) showed the Bermuda High was the highest contributor to error, the Continental High showed moderate error, while the four quadrants showed lower errors. High error cases were composited to examine potential model biases. On average, the composite showed lower balanced geopotential heights around the climatological position of the Bermuda High associated with the recurving of storms in the North Atlantic basin. The analysis techniques developed in this thesis aids in the identification of model biases which will lead to improved track forecasts in the future.

ACKNOWLEDGMENTS

The research here was possible due to the guidance, conversations, and support of many people. I am grateful for my advisor, Michael M. Bell, for passed down knowledge, guidance, and patience. His guidance and patience has played a pivotal part in my growth as a scientist. I am thankful for my internship mentor, Jan-Huey Chen, who I initially started this work with during the summer of 2021, and continued to rely on throughout my masters research. Philip J. Klotzbach, in the Bell Research group, has also been instrumental in this work with very helpful insight, research suggestions, and stimulating conversations. I am grateful for my committee members, Elizabeth A. Barnes and Yoncheng Zhou, for their comments and suggestions on this work. I'd like to acknowledge members of the Bell research group, past and present, who I've continuously complained to or bugged for help. I am thankful to all faculty, staff, and students in the Department of Atmospheric Science at Colorado State University who cultivate an inclusive and friendly environment that in turn promotes academic growth and excellence.

I have accomplished all I have today through the love, support, and guidance from countless people and cannot begin to name them all. I'd like to give thanks to and acknowledge my family, especially my father, Benny Barbero, who instilled within me my passion for science and a boundless curiosity for asking questions. To my dear friends, I thank you for listening to my long-winded attempts at explaining all things weather and oceanography. Undergraduate research experiences and coursework have been pivotal in exposing me to different topics in order to discover what I am truly passionate in. I am very grateful to my undergraduate advisor, Amato Evan, for giving me the opportunity to work as an undergraduate laboratory assistant in his lab, which provided me with my first experience in atmospheric research. I am also very thankful for Janet Becker who taught me fluid dynamics and geophysical fluid dynamics, and was the most supportive mentor during my undergraduate degree. I am thankful for funding from the Cooperative Institute for Modeling the Earth System and Princeton University for funding my internship at the Geophysical Fluid Dynamics Laboratory, in which I discovered the realm of hurricanes and tropical meteorology. Throughout my Master's, this research was supported by funding from the G. Unger Vetlesen Foundation.

TABLE OF CONTENTS

LIST OF TABLES

LIST OF FIGURES

CHAPTER 1

INTRODUCTION

1.1 STEERING FLOW

Tropical cyclones (TC) are one of the costliest and deadliest meteorological disasters, affecting many coastal and near-coastal communities. TCs that form in the Atlantic and Eastern Pacific with maximum 1-minute sustained winds >= 74 mph (64 kts), are termed hurricanes. From 1900 to 2017, a total of 207 U.S. hurricane landfalls caused over $2 trillion USD in normalized (scaled by economic inflation) damage (Weinkle et al. 2018). Thousands of direct and indirect deaths have occurred during hurricanes since the start of the 21st century. Direct fatalities are largely due to drowning from freshwater flooding, wind-driven waves, and storm surge, and physical trauma caused by airborne debris or structural failure, while indirect fatalities can occur due to trauma, carbon monoxide poisoning, and electrocution (Rappaport and Blanchard 2016).

A TC is a warm-core, low pressure system characterized by an organized, low-level circulation. Both dynamic and thermodynamic factors are required to create favorable conditions for TC formation. Energy derived from sea surface temperatures greater than 26^oC and an unstable atmosphere provides the initial ingredients for convection. Low-level rotation from an incipient disturbance or Earth's rotation is necessary to concentrate the energy into a disturbance. Low vertical wind shear and high mid-level tropospheric moisture are also necessary to sustain the development of a disturbance into a TC (Gray 1998).

To a first order, TC movement generally follows the environmental wind (i.e. advection). The environmental wind is usually associated with more than one large-scale atmospheric feature including subtropical highs, mid-latitude ridges and troughs, and low-level warm core systems (Marks 1992). The mechanism in which TC motion is steered by flow from large-scale pressure systems in the atmosphere is often known as the "cork in a stream" analogy. Subtropical highs are large-scale semi-permanent atmospheric circulations that exist in the subtropical areas of the Atlantic and Pacific Ocean basins. These highs are characterized by large-scale downward sinking motion of air, or subsidence. Subsidence is driven by the Hadley cell, a meridional overturning circulation with air rising near the equator and sinking near 30^o latitude. The subtropical high in the North Atlantic is often called the Bermuda High because during the northern hemisphere summer, it is centered around Bermuda, and its strength is typically at its maximum. The subtropical high is also sometimes called the Azores High

when the system is farther east centered over the Azores islands. The presentation of the Bermuda High is variable where the Bermuda High or Azores High is individually present, or two highs can exist simultaneously. Mid-latitude ridges and troughs are elongated areas of high pressure and low pressure, respectively. Meanders on the polar jet stream, otherwise known as Rossby waves, are created through flow interaction with terrain in the northern hemisphere. The Rossby wave crest forms a mid-latitude ridge, and the trough of a Rossby wave forms a mid-latitude trough. These mid-latitude phenomenon are typically mid- to upper-level features but their influence extends downward to the surface. The jet stream blows from west to east while Rossby waves propagate in the opposite direction. When the group speed of the Rossby waves and flow of the jet stream are approximately equal, stalls in mid-latitude ridges and troughs can arise, slowing or even halting TC motion. Lastly, the motion of a TC can also be affected by other existing nearby TCs (Fujiwhara 1921).

To a second order, TC motion is driven by the TC's internal dynamics (i.e., Beta effect). The Beta effect is a northwest drift of a TC in the northern hemisphere that is caused by vorticity gradients generated by planetary vorticity advection by the TC circulation itself. Advection and the Beta effect are the two factors that constitutes what is known as the Beta Advection Model (BAM) of TC movement (Marks 1992). As an interesting aside, binary interactions between TCs and large-scale pressure systems can occur that affect the intensity and movement of TCs. However, these interactions are tangential to the presented research and will not be discussed here. In general, TC movement is dominated by the advection component which will be solely focused on in this research.

Quantitatively, TC movement can be approximated by the response to the deep layer mean steering flow (DLMSF) which is the pressure-weighted, vertically-averaged, horizontal winds in the vicinity of the TC center (Chan and Gray 1982; Franklin et al. 1996). Both strength and proximity of the large-scale pressure system to the TC are critical to the contribution made to the DLMSF metric, but contributions from weaker systems that are farther away can also be important. From only the summation of these steering contributions, it is difficult to understand which systems contribute and how much each system contributes to the DLMSF.

1.2 Track Forecasting

TC track forecasts have improved substantially in the last several decades due to the improvement of observational quality and quantity, numerical models and data assimilation techniques (Rappaport et al. 2009). Average 3-day forecast track error in the Atlantic basin decreased by more than 2/3 from

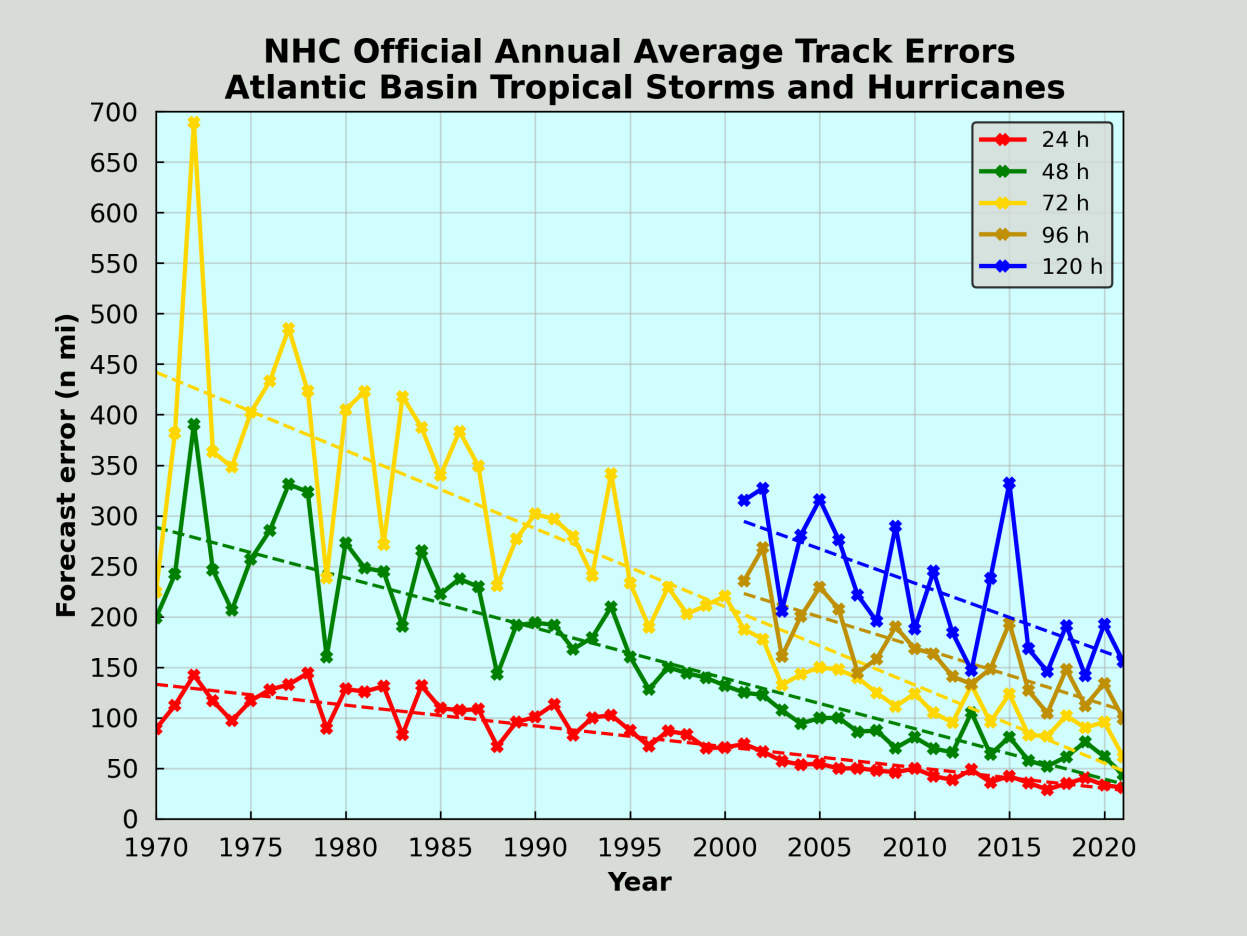

FIG. 1.1. Annual average official track errors for Atlantic basin tropical storms and hurricanes for the period 1970-2021, with least-squares trend lines superimposed. Adapted from https://www.nhc.noaa.gov/verification/verify5.shtml.

300 n mi to 100 n mi from 1990 to 2021 (Figure 1.1). Similar decreases in error are also observed at the 1-day and 2-day lead time. The aforementioned improvements also led to the National Hurricane Center (NHC) issuing predictions at 96- and 120-hrs in 2003, which have improved as well (Landsea and Cangialosi 2018).

While track errors have decreased on average significantly, large track forecast errors, such as bifurcation points and large ensemble spreads, are still observed today, and continued research into the sources of track error are imperative. However, it is difficult to understand the cause of TC track forecast errors in models. Track errors can be further reduced through additional diagnostics that identify model errors and biases.

1.3 Potential Vorticity Inversion

In this research, we utilize a novel approach to diagnosing TC steering flow errors in numerical weather prediction models. This approach involves the use of a technique called potential vorticity (PV) inversion. Mathematically, PV is the dot product of the absolute vorticity and the gradient of any scalar advected along with the fluid. If the scalar following the parcel is a function of pressure and density, PV is conserved following adiabatic (dry) and inviscid (frictionless) fluid motion for a baroclinic fluid. A baroclinic fluid is a fluid in which density is a function of temperature and pressure, in contrast to a barotropic fluid where density is only a function of pressure. While a barotropic fluid is a reasonable assumption for much of the tropical atmosphere, it is not a good assumption for the mid-latitudes or in stratified flow, where a baroclinic fluid assumption would be more appropriate. If the scalar chosen for the atmosphere is potential temperature, this formulation is called Ertel PV. Physically, Ertel PV describes the absolute circulation of a fluid parcel enclosed between two isentropic surfaces. The Ertel formulation of PV will be utilized in this thesis and more on the PV framework will be discussed in Chapter 2.2.

Since the atmosphere is a fluid, the large-scale pressure systems in the atmosphere can be regarded as large-scale PV systems. Pressure systems that rotate cyclonically (counterclockwise in the northern hemisphere) have positive PV and pressure systems that rotate anticyclonically (clockwise in the northern hemisphere) have negative PV. As such, mid-latitude troughs and ridges are systems of positive and negative PV, respectively, that are most intense at upper-levels of the atmosphere. The Bermuda High is a large-scale negative PV system that is strongest at mid levels of the atmosphere. TCs are positive PV systems that are strongest at low-levels and can span from mesoscale to synoptic spatial scales. Therefore, PV can be used as a tracer to identify large-scale atmospheric features and TCs.

The application of PV to the atmosphere as a metric to understand the evolution of weather systems in time is described by the term “PV thinking” (Hoskins et al. 1985). The comprehension of weather system development is possible due to the properties of PV: Lagrangian conservation and invertibility. In other words, 1) PV is conserved following adiabatic and inviscid motion, which is a reasonable assumption for large-scale atmospheric flow, and 2) given a spatial distribution of PV, a proper balanced condition and boundary conditions, the thermodynamic and flow fields can be retrieved.

One application of PV thinking is piecewise PV inversion (Davis 1992a), where the PV is partitioned into “pieces”, and each piece is inverted to deduce the thermodynamic and wind fields pertaining to the PV distribution. This method has been applied to the investigation of several atmospheric processes

including extratropical cyclogenesis (Davis and Emanuel 1991; Davis 1992b; Hakim et al. 1996; Huo et al. 1999), TC movement (Shapiro 1996; Wu and Emanuel 1995a,b; Wu and Kurihara 1996; Wu et al. 2003, 2004, 2012), jet movement and development (Lackmann 2002; Winters and Martin 2017; Winters et al. 2020), precipitation forcing and processes (Schlemmer et al. 2010; Baxter et al. 2011; Wang et al. 2020), and frontogenesis (Morgan 1999; Korner and Martin 2000; Chen et al. 2003).

The application of piecewise PV inversion varies depending on the atmospheric phenomenon of interest. Different variations of the perturbation definitions and PV perturbation partitioning schemes have been utilized in the aforementioned studies. For the study of hurricanes and extratropical cyclones, Davis and Emanuel (1991) defined the perturbations of Ertel PV from a time mean state averaged over a period of 5 days during the extratropical cyclone lifetime to study critical periods during extratropical cyclogenesis. Wu and Emanuel (1995a), Wu and Emanuel (1995b), and Shapiro (1996) partitioned the PV anomalies vertically to quantify the steering for different Atlantic hurricanes from PV anomalies in the lower and upper atmosphere. To study jet superposition, Winters and Martin (2017) defined the Ertel PV perturbations as a departure of the instantaneous 6-hour PV field from the 6-day mean PV field and partitioned the PV field into subtropical and polar jet PV based on pressure and relative humidity thresholds. Baxter et al. (2011) defined perturbations from a 1979–2001 climatological mean to investigate the influence of precipitation near the surface warm front on precipitation downstream. To study frontogenesis, Korner and Martin (2000) define time and perturbation means of the PV field similar to Davis and Emanuel (1991) to understand the development and frontal evolution of the cyclone that caused the infamous 1997 April Fool's Day storm in the Northeastern U.S.

1.4 Model Bias

While random errors are present in dynamical model forecasts, errors that continue to occur systematically in time, otherwise known as model biases, can also exist. Model biases can be the result of errors in the dynamics or physical parameterizations, data assimilation, initial conditions, or a combination of these. Several components work together to produce a model forecast, and it is difficult to attribute the exact cause of model biases. Furthermore, identifying the model component(s) producing the bias does not guarantee that new problems will not arise. Still, it is important to identify biases to be able to correct them and consequently improve model forecasts.

Several studies have identified model biases that are relevant to TC track. In Wu et al. (2012), the Global Forecast System (GFS) showed a northeastward track bias in Typhoon Sinlaku (2008), which was

attributed to a shallow vortex height bias. Therefore, Sinlaku did not feel the strong westward steering contribution to the DLMSF at upper levels. The track forecast better aligned with the verified track after dropwindsonde data was assimilated into the GFS forecast, and the vortex height was better reproduced. In Chen et al. (2019), the Integrated Forecast System (IFS) model run by the European Centre for Medium-Range Weather Forecasts exhibited a slow translation speed bias for Hurricanes Irma and Maria in 2017 for all forecast times. This slow bias integrates over time and contributes to track errors. Following Chen et al. (2019), we attempt to use the piecewise PV inversion diagnosis tool in identifying model biases, specifically in terms of TC track. Many previous studies have identified a single case of TC track biases using formulations of piecewise PV inversion. Yet, to the authors' knowledge, none have performed a PV analysis of an entire hurricane season for the purpose of identifying model biases. The research presented here utilizes the piecewise PV inversion tool on the 2017 Atlantic hurricane season. An extremely active hurricane season by any metric, the 2017 Atlantic hurricane season provides numerous impactful cases for analysis.

1.5 Research Objectives

The main goal of this thesis is to diagnose the sources of track error in model forecasts. To accomplish this goal, a diagnostic technique called "piecewise potential vorticity inversion" is employed. Track forecasts from four different models of storms in the 2017 Atlantic hurricane season and TC best track locations are utilized. A few intermediate objectives that accomplish the main goal are:

(1) Show that the DLMSF is a useful metric such that DLMSF errors are representative of track errors

(2) Demonstrate that the piecewise PV inversion technique can attribute track errors to DLMSF errors in certain large-scale systems

(3) Show that model biases can be identified by utilizing the piecewise PV inversion tool on an entire season

The outline of the thesis is as follows: Chapter 2 will outline the PV framework. Chapter 3 presents in-depth analysis of the case studies. Chapter 4 follows with a statistical analysis of all storms evaluated during the 2017 season. Chapter 5 finishes with a brief summary of the main points presented in this thesis and a discussion on the limitations of this work.

CHAPTER 2

METHODOLOGY

2.1 DATA AND MODELS

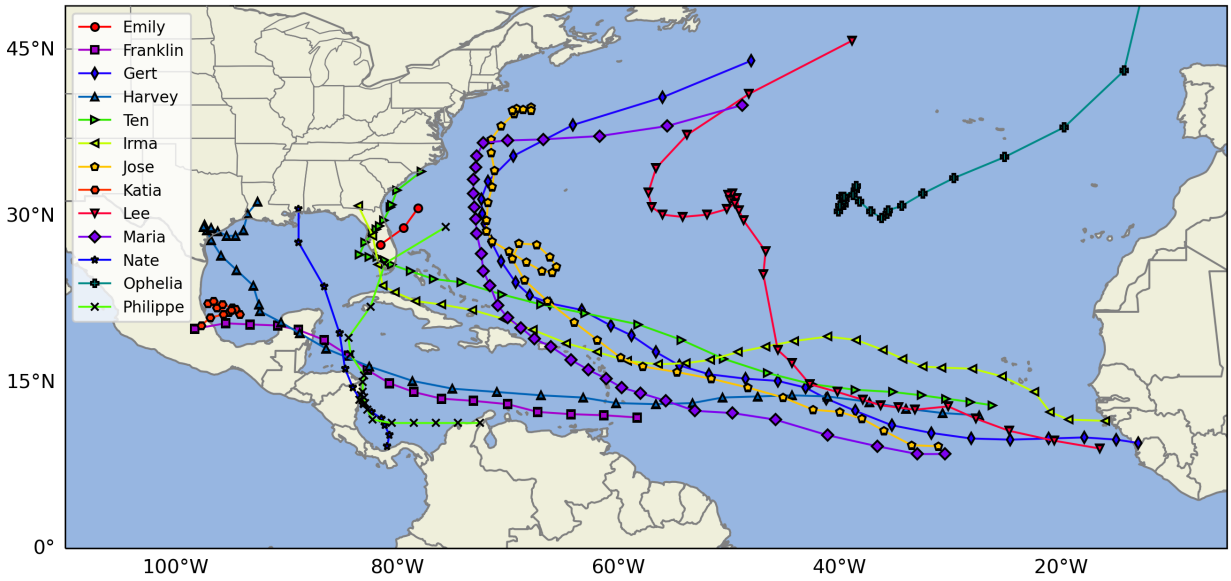

FIG. 2.1. Best tracks of tropical cyclones during the 2017 North Atlantic hurricane season.

The 2017 North Atlantic hurricane season concluded with 6 major hurricanes (category 3 and higher on the Saffir-Simpson Hurricane Wind Scale (Simpson 1974)), 10 hurricanes, and 17 named storms with the 1981-2010 median number of major hurricanes, hurricanes, and named storms being 2, 6.5, and 12 respectively (Klotzbach et al. 2018). Figure 2.1 shows the tracks of the thirteen TCs which occurred during August, September, and October of the 2017 season.

The models utilized in this study include the National Centers for Environmental Prediction (NCEP) Global Forecast System (GFS; NCEP 2016), the European Center for Medium-Range Weather Forecasts (ECMWF) Integrated Forecast System (IFS; ECMWF 2016), and the formerly named fvGFS model, now called the System for High-resolution prediction on Earth-to-Local Domains (SHiELD, Harris et al. 2020) developed by the Geophysical Fluid Dynamics Laboratory (GFDL). The SHiELD model is able to ingest initial conditions from two prominent global prediction models, the GFS and IFS (Chen et al. 2018). Henceforth, the SHiELD model forecasts run with GFS initial conditions will be labeled SHiELD gfsIC and with IFS initial conditions will be labeled the SHiELD ifsIC. A comprehensive overview of the model dynamical cores, physics suites, and native grid resolutions is shown in Table 2.1.

TABLE 2.1. Comparison of the previously operational NCEP GFS, the GFDL fvGFS, and the ECMWF IFS. Adapted from Chen et al. (2019).

	NCEP GFS	**ECMWF IFS**	**GFDL SHiELD**
Dynamical core	Hydrostatic spectral model with semi-implicit semi-Lagrangian horizontal discretization and three-dimensional Hermite interpolation	Hydrostatic spectral model with semi-implicit semi-Lagrangian horizontal discretization and finite element vertical discretization	Nonhydrostatic finite-volume cubed-sphere dynamical core (FV3)
Physics suite	GFS	IFS	Updated GFS with the GFDL microphysics, the YSU PBL, and a mixed-layer ocean model
Model resolution	13 km/64 levels	9 km/137 levels	13 km/91 levels
Initial conditions	GFS	IFS	GFS/IFS

The native grid resolution and vertical levels are re-gridded to a 1° by 1° global latitude longitude grid and 25 vertical levels for all models. The 10-day forecasts are initialized every 12 hours from 1 August 2017 to 31 October 2017 and are run every 6 hours. The GFS and IFS analysis data at 00, 06, 12, and 18 UTC for the same time period are used to compare to forecasts. A subset of the global grid is defined on which the analyses are performed and ranges from 0° to 55°N and 110°W to 5°W. This new grid encompasses the regions of interest which include the North Atlantic and part of the continental United States.

TC track errors are computed by comparing the model forecast TC locations against their verified positions in the Automated Tropical Cyclone Best Track data set (Miller et al. 1990; Sampson and Schrader 2000).

2.2 POTENTIAL VORTICITY FRAMEWORK

The dynamical framework used in this study follows Wu et al. (2003). Ertel PV (Rossby 1940; Ertel 1942) is defined as:

$$q = \frac{1}{\rho}(\zeta + f)\frac{\partial \theta}{\partial p}, \tag{2.1}$$

where q is Ertel PV, ζ is relative vorticity, f is the Coriolis parameter, ρ is the fluid density, θ is potential temperature, and p is the pressure coordinate. The PV is inverted using the nonlinear balanced equation (Charney 1955):

$$\nabla^2\Phi = \nabla \cdot f\nabla\Psi + 2\,[\frac{\partial^2\Psi}{\partial x^2}\frac{\partial^2\Psi}{\partial y^2} - (\frac{\partial^2\Psi}{\partial x \partial y})^2], \tag{2.2}$$

where Φ is the geopotential, Ψ is the stream function for the non-divergent wind, and the divergence and gradient operators are two-dimensional in the horizontal. In short, Ertel PV is a quantity that measures the absolute vorticity and the static stability of a fluid column and is conserved for three-dimensional, adiabatic (dry), inviscid (frictionless) motion. The nonlinear balanced relation holds well for large-scale atmospheric flow where horizontal motions dominate over vertical motions and flow is mainly non-divergent (i.e., no large vertical accelerations in the flow). To solve the equations for the real atmosphere, the system is re-formulated on the π ($\pi = C_p(\frac{p}{p_o})^\kappa$) vertical coordinate and spherical horizontal coordinates. The horizontal wind within the absolute vorticity in Equation 2.1 is also replaced by the non-divergent wind and the PV can be rewritten as:

$$q = \frac{g\kappa\pi}{p}\,[(f+\nabla^2\Psi)\frac{\partial^2\Phi}{\partial\pi^2} - \frac{1}{a^2 cos^2\phi}\frac{\partial^2\Psi}{\partial\lambda\partial\pi}\frac{\partial^2\Phi}{\partial\lambda\partial\pi} - \frac{1}{a^2}\frac{\partial^2\Psi}{\partial\phi\partial\pi}\frac{\partial^2\Phi}{\partial\phi\partial\pi}], \tag{2.3}$$

where q is PV, Φ is now the geopotential height, Ψ is stream function, a is earth's radius, f is the Coriolis parameter, $\kappa = \frac{R_d}{C_p}$, λ is longitude, and ϕ is latitude. Equation 2.2 can be rewritten as:

$$\nabla^2\Phi = \nabla\cdot(f\nabla\Psi) + \frac{2}{a^4 cos^2\phi}\frac{\partial(\partial\Psi/\partial\lambda, \partial\Psi/\partial\phi)}{\partial(\lambda,\phi)}, \tag{2.4}$$

where Φ is the geopotential height, Ψ is stream function, a is earth's radius, f is the Coriolis parameter, λ is longitude, and ϕ is latitude. The complete system is solved in Equation 2.3 and Equation 2.4 for the unknowns of Φ and Ψ. Given a distribution of q, Φ and Ψ on the horizontal boundaries, and θ ($\theta = -\frac{\partial\Phi}{\partial\pi}$) on the upper and lower boundaries, the distribution of Φ and Ψ can be solved using successive over- and under-relaxation (Davis and Emanuel 1991).

Another type of PV is quasi-geostrophic PV (QGPV); however, Ertel PV is utilized here rather than QGPV because the accuracy of the QGPV inversion decreases as the Rossby number approaches unity. The Rossby number is a dimensionless ratio between the inertial to Coriolis forces in a rotating fluid. A common formulation of the Rossby number is $Ro = \frac{U}{fL}$, where U is a characteristic velocity, f is the Coriolis parameter, and L is a characteristic horizontal length scale. Large Rossby numbers may occur

in highly rotational flows such as in TCs (Davis 1992a). A number of studies have shown the utility of the Ertel PV and nonlinear balance equation framework in studying TC movement and cyclogenesis (Davis and Emanuel 1991; Wu and Emanuel 1995a,b; Shapiro 1996; Wu et al. 2003, 2004).

The disadvantage of the framework that we have adopted from Wu et al. (2003) is that the system being solved (Ertel PV and the nonlinear balance equation) is highly nonlinear. In other words, the sum of the piecewise PV perturbations does not add up to the total, which introduces ambiguity in the inversion interpretation. To compensate, the full linear method is applied which hides the nonlinear terms within the linear terms by incorporating the nonlinear terms in a non-constant coefficient linear differential operator. This method effectively linearizes the system and removes interpretation ambiguity (Davis and Emanuel 1991). Davis (1992a) reviewed several methods to linearize the system, but ultimately showed that keeping the nonlinear terms in PV perturbation equations is essential to the accuracy of the inversion.

For this research, we use the PV decomposition described in Shapiro (1996). The axisymmetric vortex in a 2000 km radius around the TC center is calculated as the basic field and perturbations are defined as deviations from the basic field. Firstly, the basic wind field is computed to obtain the basic stream function $\overline{\Psi}$. The nonlinear balance equation is used to calculate the basic geopotential height Φ:

$$\nabla^2\hat{\Phi} = \nabla\cdot(f\nabla\overline{\Psi}) + \frac{2}{a^4 cos^2\phi}\frac{\partial(\partial\overline{\Psi}/\partial\lambda, \partial\overline{\Psi}/\partial\phi)}{\partial(\lambda,\phi)}. \tag{2.5}$$

The $\hat{\Phi}$ notation indicates that it is not the azimuthally averaged geopotential height field, rather, it is the geopotential height field in balance with the azimuthally averaged stream function which we call the basic geopotential height. Then, the basic PV field can be calculated by Equation 2.3, but substituting the basic fields in for the total fields:

$$\hat{q} = \frac{g\kappa\pi}{p}[(f+\nabla^2\overline{\Psi})\frac{\partial^2\hat{\Phi}}{\partial\pi^2} - \frac{1}{a^2 cos^2\phi}\frac{\partial^2\overline{\Psi}}{\partial\lambda\partial\pi}\frac{\partial^2\hat{\Phi}}{\partial\lambda\partial\pi} - \frac{1}{a^2}\frac{\partial^2\overline{\Psi}}{\partial\hat{\phi}\partial\pi}\frac{\partial^2\hat{\Phi}}{\partial\phi\partial\pi}] \tag{2.6}$$

The Shapiro decomposition is appropriate here because it cleanly separates the TC from its environment, allowing us to understand how the environment (i.e., PV perturbations) affects TC movement. It is important to note that the choice of decomposition is dependent on the atmospheric application. Next, the perturbation fields can be computed by subtracting the basic fields from the total fields as:

$$\Psi' = \Psi - \overline{\Psi}, \quad \Phi' = \Phi - \hat{\Phi}, \quad q' = q - \hat{q} \tag{2.7}$$

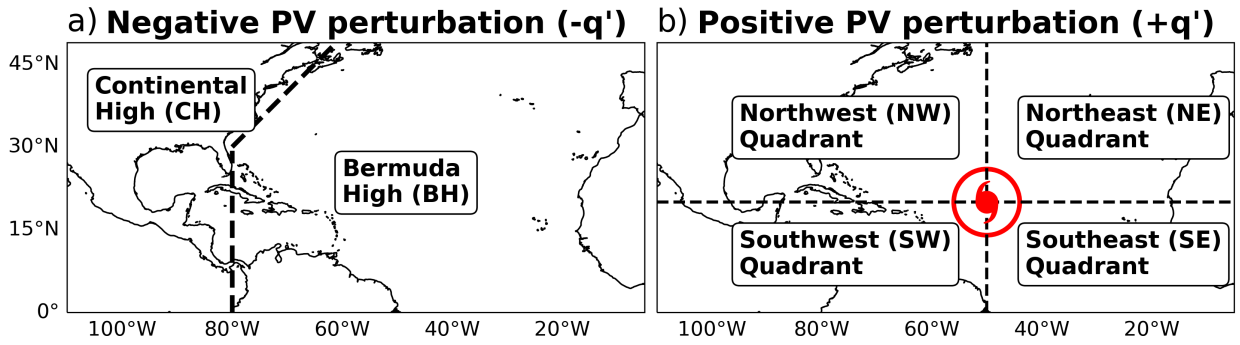

FIG. 2.2. Decomposition of the total PV perturbation field split geographically into positive and negative anomalies. a) Negative PV perturbations are divided into the Continental High and Bermuda High. A meridional line at 80°W extending from 0° to 30° N connected to a diagonal line approximately parallel to the United States's East Coast separates the PV systems. b) Positive PV perturbations are divided into the northwest, northeast, southeast, and southwest quadrants relative to the center of the TC at each point in time.

Finally, from the q' (i.e., the "full" PV perturbation field), a piecewise partitioning can be applied.

The piecewise partitioning of the PV perturbation field (i.e., anomalies) is also highly dependent on the atmospheric feature of interest. For this study, we break up the PV anomalies geographically by sign (Figure 2.2). All negative PV anomalies are divided by a meridional line at 80°W extending from 0° to 30°N connected to a diagonal line approximately parallel to the United States's East Coast. The division line was subjectively determined with the intent to isolate negative PV anomalies from the semi-permanent subtropical high (Bermuda High) located over the North Atlantic from the semi-permanent high located over the continental United States (Continental High). All positive PV anomalies are divided into four quadrants: northwest (NW), northeast (NE), southeast (SE), and southwest (SW), relative to the TC center at each point in time. This simple division of the low PV into four storm-relative quadrants provides an efficient and practical way to attribute steering flow to these systems instead of tracking the low PV anomalies individually. Overall, the full PV perturbation field is partitioned into six regions where the sum of the pieces equals the total:

$$q'_{total} = q'_{BH} + q'_{CH} + q'_{NW} + q'_{NE} + q'_{SE} + q'_{SW} \tag{2.8}$$

where BH is the Bermuda High and CH is the Continental High. Individual PV perturbation pieces are inverted to obtain the corresponding balanced Φ and Ψ fields, globally. The balanced fields describe

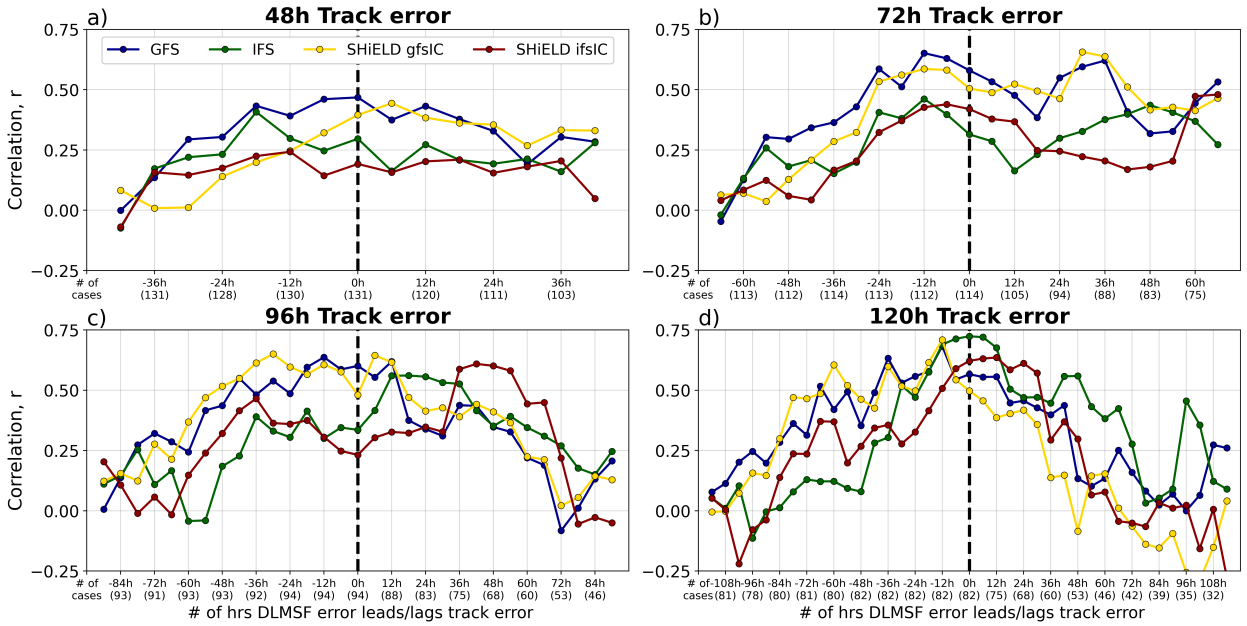

FIG. 2.3. DLMSF error and track error correlation plots. The DLMSF error varies relative to the track error at a static forecast hour. The correlations are shown for different static forecast hours: a) 48h, b) 72h, c) 96h, and d) 120h.

how a PV distribution influences the atmospheric flow in the form of a stream function and geopotential height field. From the stream function, the non-divergent, horizontal wind field (V) can be computed at each atmospheric level from the following relation:

$$V = \hat{k} \times \nabla \Psi. \tag{2.9}$$

2.3 BRIDGING TRACK ERROR AND STEERING FLOW

In order to understand how the TC is steered by its large-scale environment, the deep layer mean steering flow (DLMSF) is calculated. The DLMSF is defined as the 925 to 300 hPa layer-mean, balanced, horizontal wind field in a 3^o radius around the TC center. The DLMSF is calculated for each of the balanced wind field regions for the entire forecast time, which we will define as $DLMSF(q'_{sys})$, where q' is the PV perturbation field corresponding to a specific system (e.g., Bermuda High).

The objective of this study is to diagnose the sources of track error in model forecasts. Errors in the wind field surrounding the TC will cause errors in the track forecast. Therefore, we use DLMSF error as a proxy for track error. The correlation between the DLMSF error at varying lead times to track errors are shown in Figure 2.3 at different static lead times. The correlation was calculated using homogeneous cases, or in other words, a forecast case that is run for all of the models initialized at the same time.

The DLMSF error and track error correlations are moderately high with a Pearson correlation coefficient of 0.5-0.75 for the 72-, 96-, and 120-hr static forecast times and weaker correlations of around 0.25-0.50 for the 48-hr static forecast time. The correlation plots generally show a maximum at -24 to 0 hours, meaning track errors at a certain lead time are generally caused by errors in the TC DLMSF up to 24 hours before. The time interval for the maximum correlation is reasonable, as it takes time for steering errors to accumulate and cause errors in the position at later forecast times. Interestingly, when DLMSF error lags track error (i.e., positive hours), the correlation does not immediately decrease to zero. A probable reason is that storms that are forecast in the wrong place (i.e., track error) will lead to errors in the steering flow (i.e., DLMSF errors), and therefore track errors leading DLMSF errors will be correlated.

The 48-hr correlation plot shows the lowest maximum correlation values out of all of the correlation plots. Generally, the maximum correlation increases with increasing lead time. At earlier lead times, models tend to perform relatively well, which means DLMSF errors and track errors are low and have not had sufficient time to cause errors in the other field. At later lead times, errors may have had time to develop and cause errors in each other's field, explaining the increasing maximum correlation with increasing lead time in the correlation plots.

While the correlations between track errors and DLMSF errors are relatively high, the correlations are not perfect, meaning that the DLMSF error is an imperfect proxy for track error. The discrepancy between the two could be due to the representation of the DLMSF and how our methodology only considers advection, simplifications in the PV inversion methodology, or other factors. An elaboration of the DLMSF limitations will be discussed in section 5. Overall, the moderate correlations between the DLMSF error and the track error show that our defined DLMSF is a sufficient proxy for the forecasted movement of a TC, and that DLMSF errors are representative of track errors.

CHAPTER 3

CASE STUDY ANALYSES

The utility of the piecewise PV inversion diagnostic will be shown for three case studies of hurricanes (Harvey, Irma, and Maria) within different steering environments. For each case, a 5-day track forecast exhibiting distinctive track errors is chosen and analyzed.

3.1 CASE STUDY: HURRICANE HARVEY

On 26 August 2017 0300Z, Hurricane Harvey made landfall as a category 4 (on the Saffir-Simpson Hurricane Wind scale) on the central Texas coastline. As Harvey approached the coastline of Texas, its northward movement slowed to an eventual stall. Harvey's proximity to the Gulf of Mexico at the time of its stall provided optimal conditions for moisture transport from the Gulf of Mexico over land, resulting in several feet of rainfall in population dense regions of southeastern Texas including the Houston metropolitan area (Blake and Zelinsky 2018; DeHart and Bell 2020). However, the forecasted track of Harvey by various models exhibited errors in both speed and direction, and differences in northward translation speed or landfall position would likely have resulted in vastly different societal impacts.

Figure 3.1 shows Harvey's 5-day track forecast initialized on 24 August 2017 0Z with 6-hourly forecasts and coinciding Best Track (BT) positions. By comparing the model track forecasts to the BT, we see that none of the models forecast every aspect of Harvey's track correctly. By 6h, three of the four models lagged behind the BT, except for the IFS. From 6h to 48h, all models showed a distinct westward track error compared to the BT. After 48h, distinct differences between the individual models arise. The GFS exhibited a track farther to the southwest, with a slowdown and stall verifying fairly far away from the observed track. The IFS shows a similar stall to the BT subsequent to landfall, but showed Harvey backtracking almost parallel to the direction from where it made landfall instead of advecting Harvey to the east. The SHiELD gfsIC and SHiELD ifsIC models both showed a stall, followed by eastward advection. None of the models got every aspect of Harvey's track correct, but they all exhibit a stall as it crossed over land. While the IFS and SHiELD models moved approximately in the correct direction, the GFS stalled drastically southwest of the other models and the BT. For this case, the piecewise PV inversion tool is used to diagnose the southwest track error in the GFS and will be compared to the SHiELD gfsIC, which performed relatively well. The other errors mentioned above will be discussed in the DLMSF analysis.

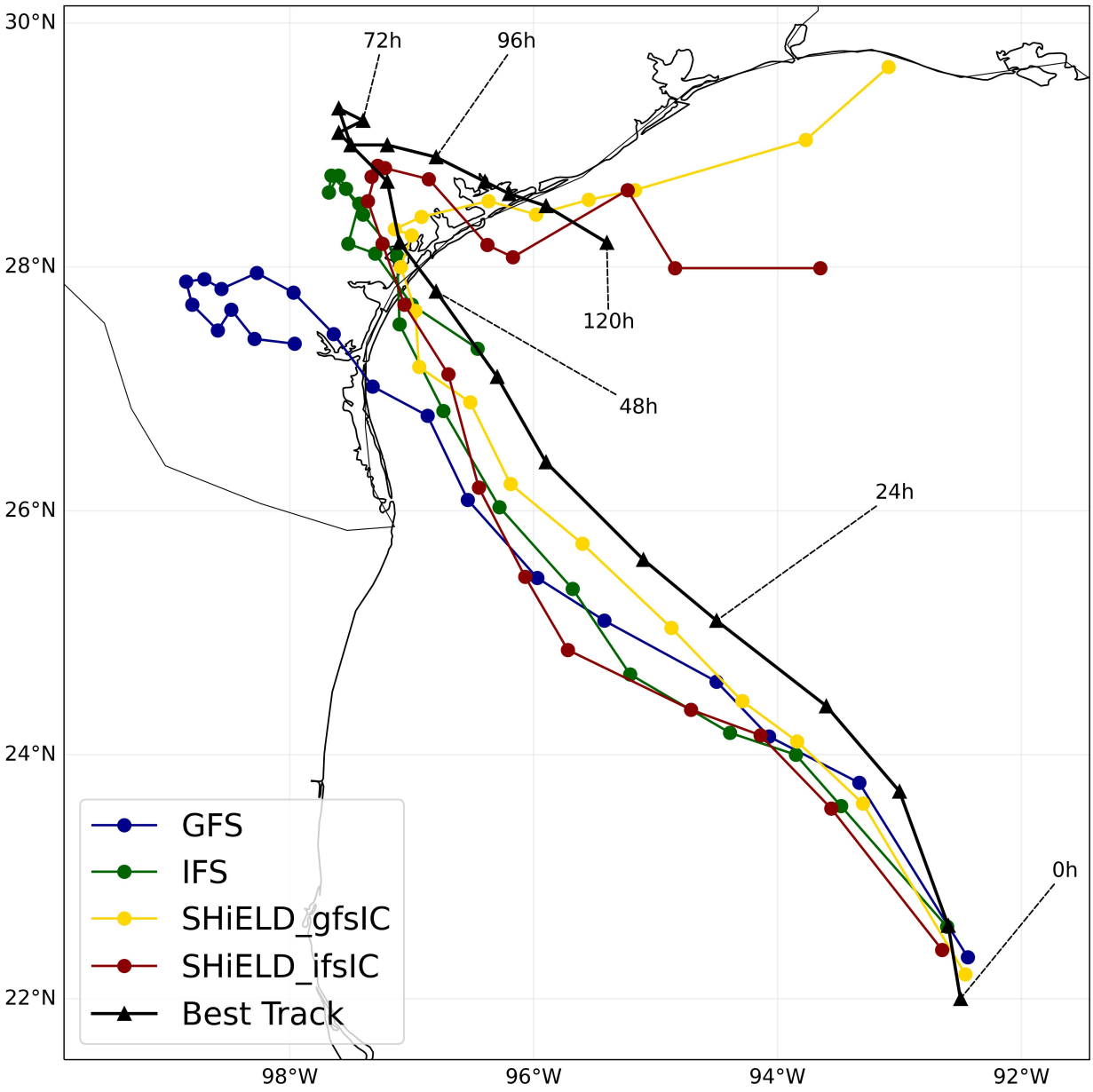

FIG. 3.1. Hurricane Harvey 5-day track forecast and best track positions. The track forecast positions start at 6 hours and are plotted every 6 hours. The best track positions start at 0 hours on 24 August 2017 and are plotted every 6 hours.

An overview of the errors in the steering flow surrounding Harvey is shown in plots of the differenced 500 hPa, balanced, geopotential heights and 925-300 hPa layer-mean horizontal wind. The analysis field synoptic setup around Harvey at 72h in Figure 3.2a showed that Harvey was located between two high pressure systems: a high located over the Four Corners region to the northwest, and a high pressure system located over the North Atlantic subtropics to the east. The two highs created opposing,

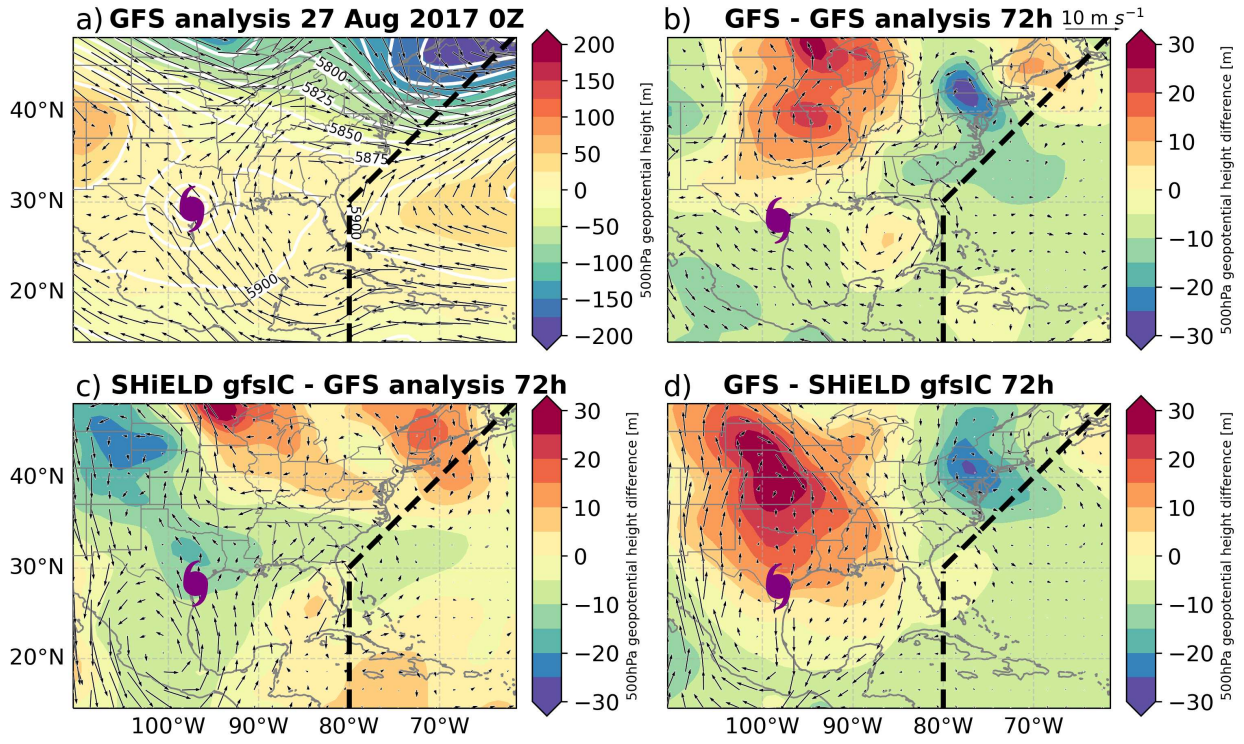

FIG. 3.2. Overview of the synoptic features surrounding Harvey at 72h. 500 hPa balanced geopotential heights (m) are shaded. 925-300 hPa layer-mean balanced wind fields are illustrated by the arrows (ms^{-1}). The thick, dashed line represents the static boundary separating the Continental High and Bermuda High regions. At 72h, (a) shows the GFS analysis fields as well as 500 hPa total geopotential height field overlaid (contours), and (b), (c), (d) shows the differenced fields for GFS forecast - GFS analysis, SHiELD gfsIC - GFS analysis, and GFS - SHiELD gfsIC forecasts, respectively.

anticyclonic circulations, resulting in a weak steering environment in Harvey's near-environment flow. A weak low pressure system to the southwest is discernible with weak cyclonic flow, but this low pressure system was not readily apparent in the mid-level geopotential height field. Another low pressure system was located over the northeastern U.S., but this system was likely too distant to play a major role in Harvey's steering.

Errors in the strength and location of these large-scale systems likely resulted in forecast track errors. Figure 3.2b shows the error of the 72h GFS forecast. The main factor driving Harvey's southwest track error is the presence of higher heights and stronger anticyclonic flow associated with the Continental High to the north. This flow blocked Harvey's path northward and instead steered Harvey towards the west. Lower heights and stronger cyclonic flow associated with a low to the south also steers Harvey to the west. However, the influence from the low likely does not play a large part in Harvey's southwest track error as the low is weak in strength. The SHiELD gfsIC forecast error is shown in

Figure 3.2c. The forecast shows weaker heights collocated with stronger cyclonic flow compared to the analysis, but the height differences are small relative to the GFS forecast error. The small difference in steering flow in the SHiELD gfsIC allows for a track forecast that better follows the BT. The GFS minus SHiELD gfsIC forecast difference is shown in Figure 3.2d. The GFS forecast shows much higher heights than the SHiELD gfsIC, which contributes north-northeastward steering over Harvey, confirming the southwest track error in the GFS.

From the balanced wind fields from each system for the GFS and SHiELD gfsIC forecasts, as well as the GFS analysis, the DLMSF is calculated and is shown in Figure 3.3. Note that the y-axes on Figure 3.3 which represents the absolute value of the u- and v-components of DLMSF range in magnitudes but are all plotted on the same scale. The identical scaling allows for easy comparison between the DLMSF values of different subplots. The southwest track deviation in the GFS should be caused by errors in the u component of DLMSF (u-DLMSF), generally after 72h. The NE quadrant shows weaker westerly flow and the Continental High, Bermuda High, and NW, SW, SE quadrants all show stronger easterly flow. The sum contribution of these errors in the DLMSF cause Harvey's southwest track deviation in the GFS. While both models show an error in the u-DLMSF, the Continental High and the NE quadrant are the main producers of the error and contribute an average of 1 ms^{-1} and 0.5 ms^{-1} respectively, with smaller contributions from the Bermuda High, and NW, SW, and SE quadrants (Figure 3.4). The DLMSF forecast errors are computed by subtracting the DLMSF forecast from the analysis field using the same initial conditions. For example, the GFS and SHiELD gfsIC forecasts are both initialized with GFS initial conditions, thus the errors in the GFS and SHiELD gfsIC forecasts are calculated against the GFS analysis fields.

The DLMSF can diagnose the others errors in the track forecast as well. After 72h, the SHiELD gfsIC displayed strong eastward advection relative to the BT. The strong eastward movement should be caused by errors in the u-DLMSF, namely, a stronger positive u-DLMSF (e.g., stronger westerlies) or weaker, negative u-DLMSF (e.g., weaker easterlies). The NE and NW quadrants, and the Bermuda High all showed a westerly DLMSF that was stronger compared to the BT while the SE and SW quadrants, and the Continental High all showed an easterly DLMSF that was weaker compared to the BT after 72h. The main contributors to the DLMSF error are the Continental High contributing around 2 ms^{-1} and the NE quadrant contributing around 0.75 ms^{-1} of DLMSF error as shown in Figure 3.4. The other systems also produce smaller amounts of DLMSF error, typically less than 0.25 ms^{-1}.

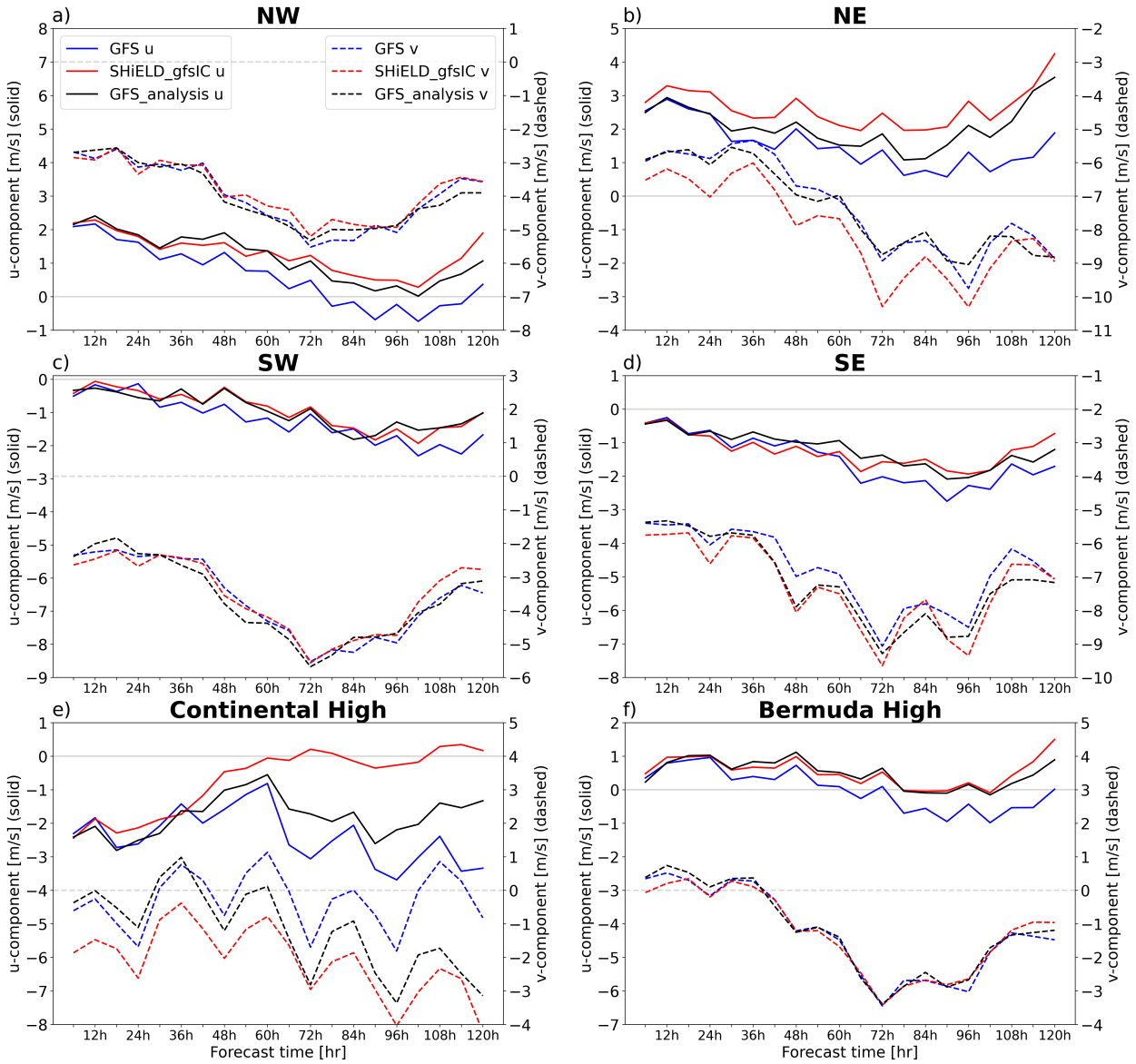

FIG. 3.3. Plots of the Deep Layer Mean Steering Flow (DLMSF, ms^{-1}) for Harvey. a), b), c), d), e), f) represents the DLMSF from the NW quadrant, NE quadrant, SW quadrant, SE quadrant, Continental High, and the Bermuda High, respectively. The blue lines are the GFS DLMSF, the red lines are the SHiELD gfsIC DLMSF, and the black lines are the GFS analysis DLMSF. Gray horizontal lines represent the zero-line for each axis. Solid lines represent the u-component of DLMSF, and dashed lines represent the v-component of DLMSF.

The tracks from 6h to 48h for both the GFS and SHiELD gfsIC were forecast west of the BT, which should be caused by errors in the u-DLMSF during these lead times. A stronger, negative u-component (e.g., stronger easterlies) or a weaker, positive u-component (e.g., weaker westerlies) cause a westward track error. For both models from 6h to 48h, the NW, NE quadrants, and the Bermuda High show westerly DLMSF, while the SW, SE quadrants, and the Continental High show easterly DLMSF on Harvey.

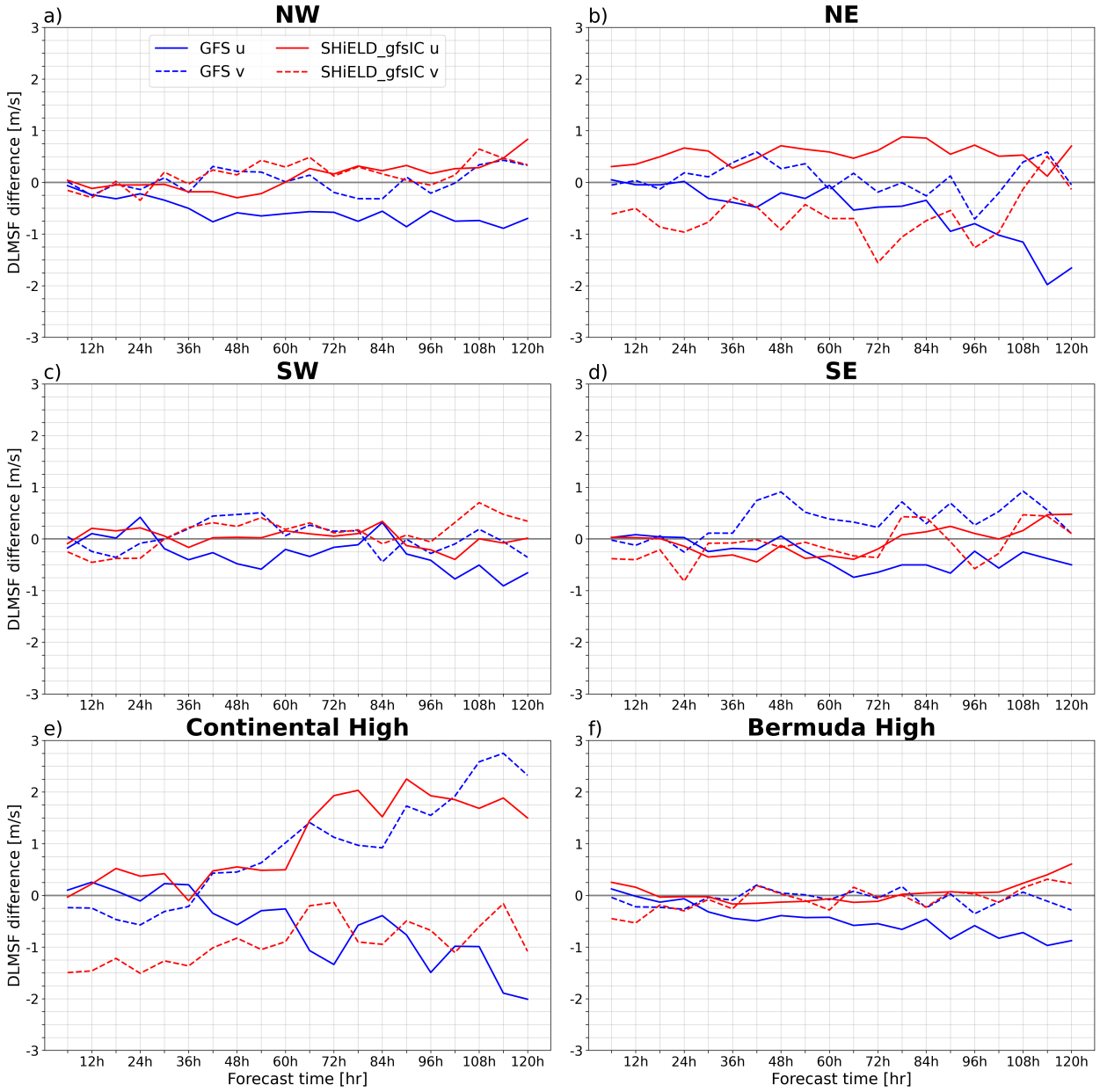

FIG. 3.4. Plots of the forecast minus analysis Deep Layer Mean Steering Flow (DLMSF, ms^{-1}) for Harvey. a), b), c), d), e), f) represents the DLMSF difference from the NW quadrant, NE quadrant, SW quadrant, SE quadrant, Continental High, and the Bermuda High, respectively. The blue lines show the GFS, and the red lines show the SHiELD gfsIC. Solid lines show the u-component of DLMSF, and dashed lines show the v-component of DLMSF.

In Figure 3.4, the GFS DLMSF differences are mostly negative for the NW, NE quadrants, and Bermuda High which indicates weaker westerly DLMSF from these systems. The GFS DLMSF differences are also mostly negative for the SW, SE quadrants, and the Continental High which shows stronger easterlies from these systems. These errors are consistent with the westward track error from 6h to 48h in the

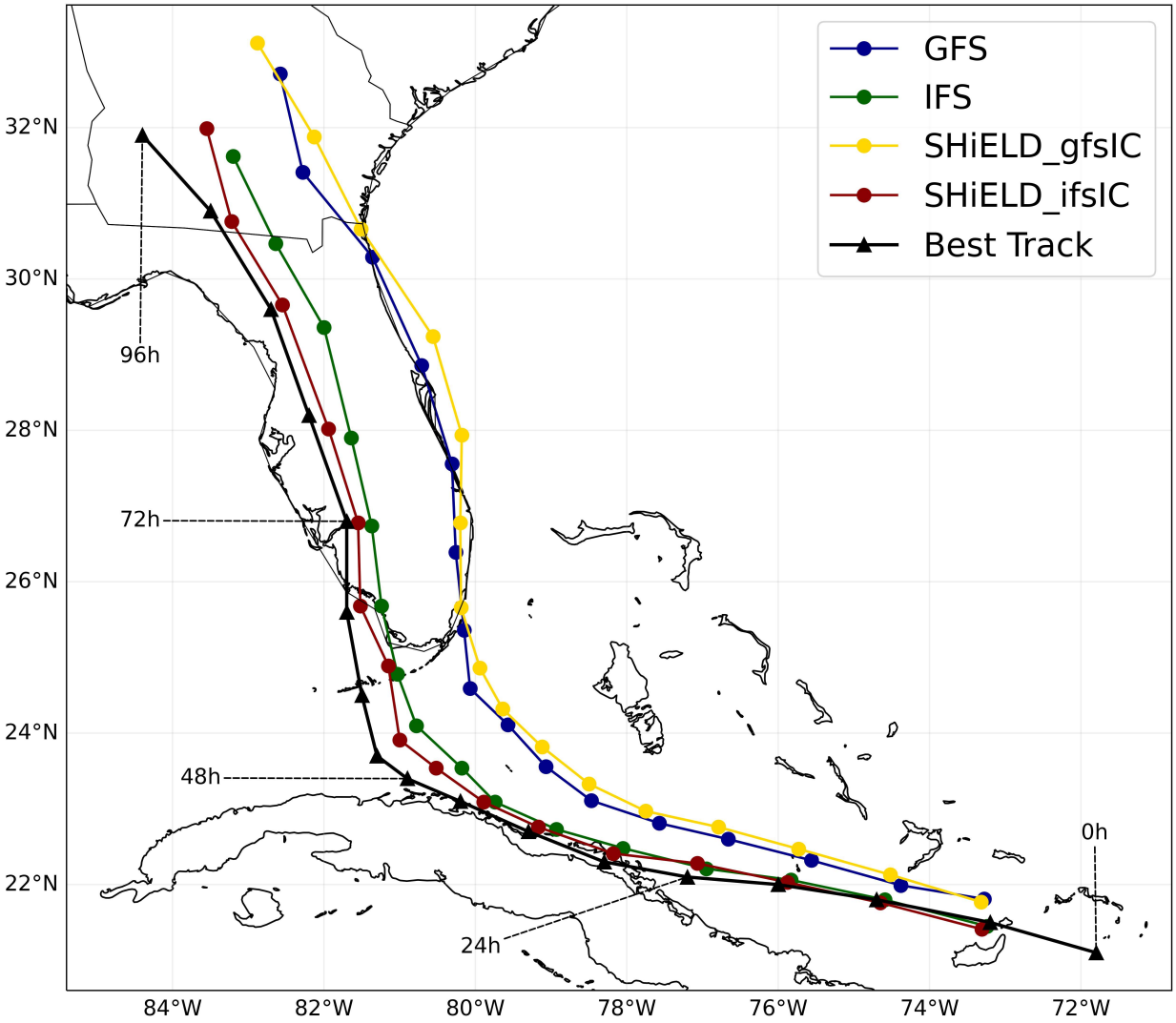

FIG. 3.5. As in Figure 3.1 but for Hurricane Irma. The tracks stop at 96h due to Irma being declared a remnant low at that time. The track forecast was initialized on 8 September 2017 0Z.

GFS. However, the same cannot be said about the SHiELD gfsIC. The u-DLMSF errors for the SHiELD gfsIC are not consistent with its westward track error during the same time period. This may be indicative of other factors playing a role in Harvey's track such that the DLMSF metric does not fully represent Harvey's movement.

3.2 CASE STUDY: HURRICANE IRMA

Hurricane Irma was a powerful Category 5 hurricane that caused devastation to several Caribbean islands including Cuba as well as portions of Florida. Its track was governed by a combination of steering from the Bermuda High, Continental High, a distant, mid-latitude trough to the northeast, and a

developing low to its northwest (Cangialosi et al. 2021). Like Harvey, differences in Irma's forecast track would have caused Irma to have drastically different impacts.

Figure 3.5 shows the 5-day track forecast for Irma every 6 hours initialized on 8 September 2017 0Z along with the corresponding BT positions. By 6h, the forecasts began to diverge from each other, although models run with the same initial conditions had similar tracks. The models run with GFS initial conditions showed a northward track error as well as a slight slow translation speed error, while the models run with IFS initial conditions generally followed the BT. The northward track error and slow translation speed error of Irma in the SHiELD gfsIC will be compared to the relatively well forecasted track in the SHiELD ifsIC.

The synoptic-scale features influencing Irma's movement at 24h are shown in Figure 3.6. The analysis fields show three main systems: a high pressure to the east, a high pressure to the west, and a trough to the north. Steering flow in the near surrounding of Irma was largely southeasterly, dominated by influence from the Bermuda High to its east.

The SHiELD gfsIC forecast error is shown in Figure 3.6c. A dipole of weaker heights to the west and higher heights to the east was collocated with stronger southerly steering, which supports the northward track error in the SHiELD gfsIC. The SHiELD ifsIC forecast error in Figure 3.6d also shows differences in the height field, but these differences are smaller compared to the SHiELD gfsIC. These smaller differences in the SHiELD ifsIC do not manifest into a northward track error as the SHiELD gfsIC does.

The DLMSF from each system for the SHiELD gfsIC and SHiELD ifsIC during the 5-day forecast and analysis runs are shown in Figure 3.7. In order to address the northward track error in the SHiELD gfsIC, the analysis is split from 6h to 48h, when Irma's motion is predominately westward, and 48h onward in which Irma's motion is generally northward. This separation is intuitive because the component of DLMSF that caused the error depends on the direction of motion of the storm. The 6-48h interval is focused on in the following analysis.

It is reasonable to assume that errors in the v component of DLMSF (v-DLMSF) from the various systems should result in meridional track differences. Figure 3.8 shows large v-DLMSF errors in the Continental High and Bermuda High which both contribute around 0.25-0.75 ms^{-1} v-DLMSF error compared to less than 0.25 ms^{-1} v-DLMSF error from the quadrants. The SHiELD gfsIC shows a stronger v-DLMSF than the GFS analysis for both the Bermuda High and Continental High. However, the Continental High v-DLMSF is strictly negative (e.g., northerly flow) and the Bermuda High v-DLMSF is strictly positive (e.g., southerly flow). While the two systems exhibit comparable errors,

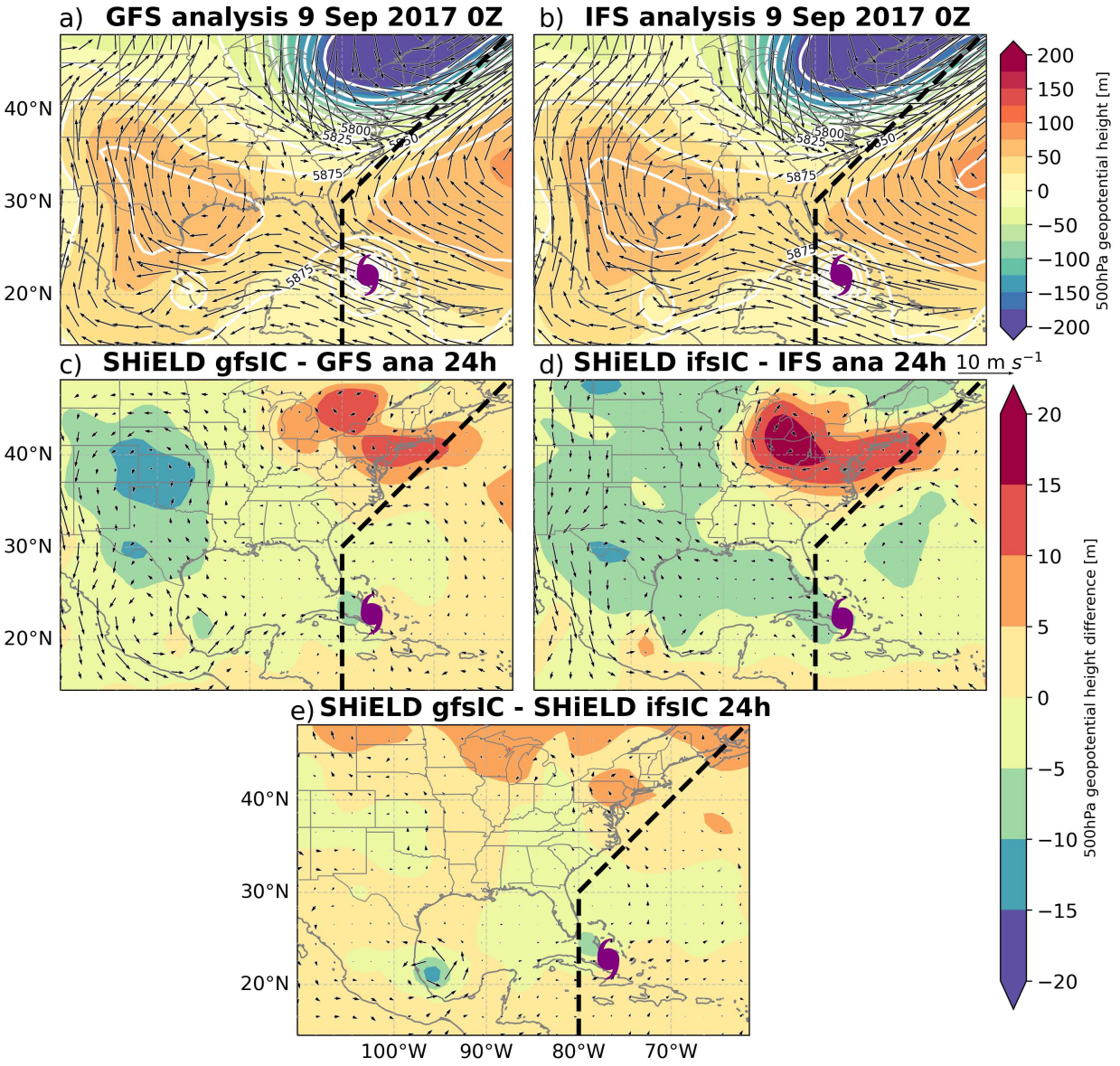

FIG. 3.6. As in Figure 3.2 but for Hurricane Irma at 24h.

southerly flow from the Bermuda High is larger in magnitude by 1-2 ms^{-1} than the northerly flow from the Continental High. This resulted in a net southerly contribution to the total DLMSF resulted in the northward track error in the SHiELD gfsIC.

Stronger positive u-DLMSF (e.g., stronger westerlies) or weaker negative u-DLMSF (e.g., weaker easterlies) caused the slow translation speed error in the SHiELD gfsIC. The Bermuda High, Continental High, and SE and SW quadrants contribute easterly steering, while the NW and NE quadrants contribute westerly steering on Irma. Figure 3.8 shows that the largest contributors to the u-DLMSF error are the Bermuda High, the Continental High, and the NW and NE quadrants contributing around

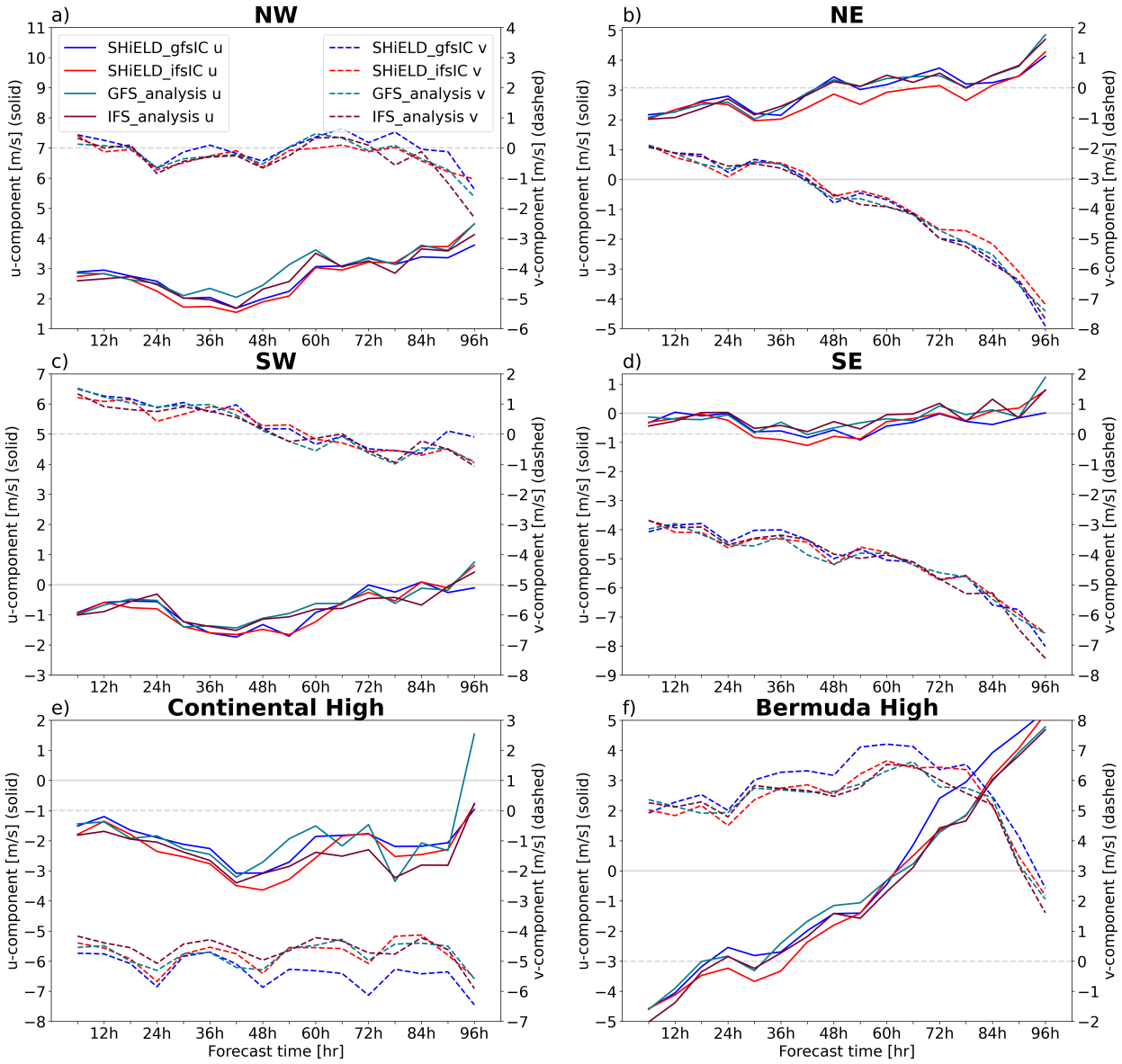

FIG. 3.7. As in Figure 3.3 but for Hurricane Irma.

0.5 ms^{-1} u-DLMSF error each, with less than 0.25 ms^{-1} u-DLMSF error being contributed by the other systems. Overall, the slow translation speed error is due to a combination of DLMSF from different systems at various lead times contributing flow counteracting Irma's westward movement and causing the slow translation speed error.

3.3 CASE STUDY: HURRICANE MARIA

Hurricane Maria was a devastating hurricane that made landfall in Dominica as a Category 5 hurricane, followed by a second landfall in Puerto Rico at Category 4 intensity. Maria also posed a significant

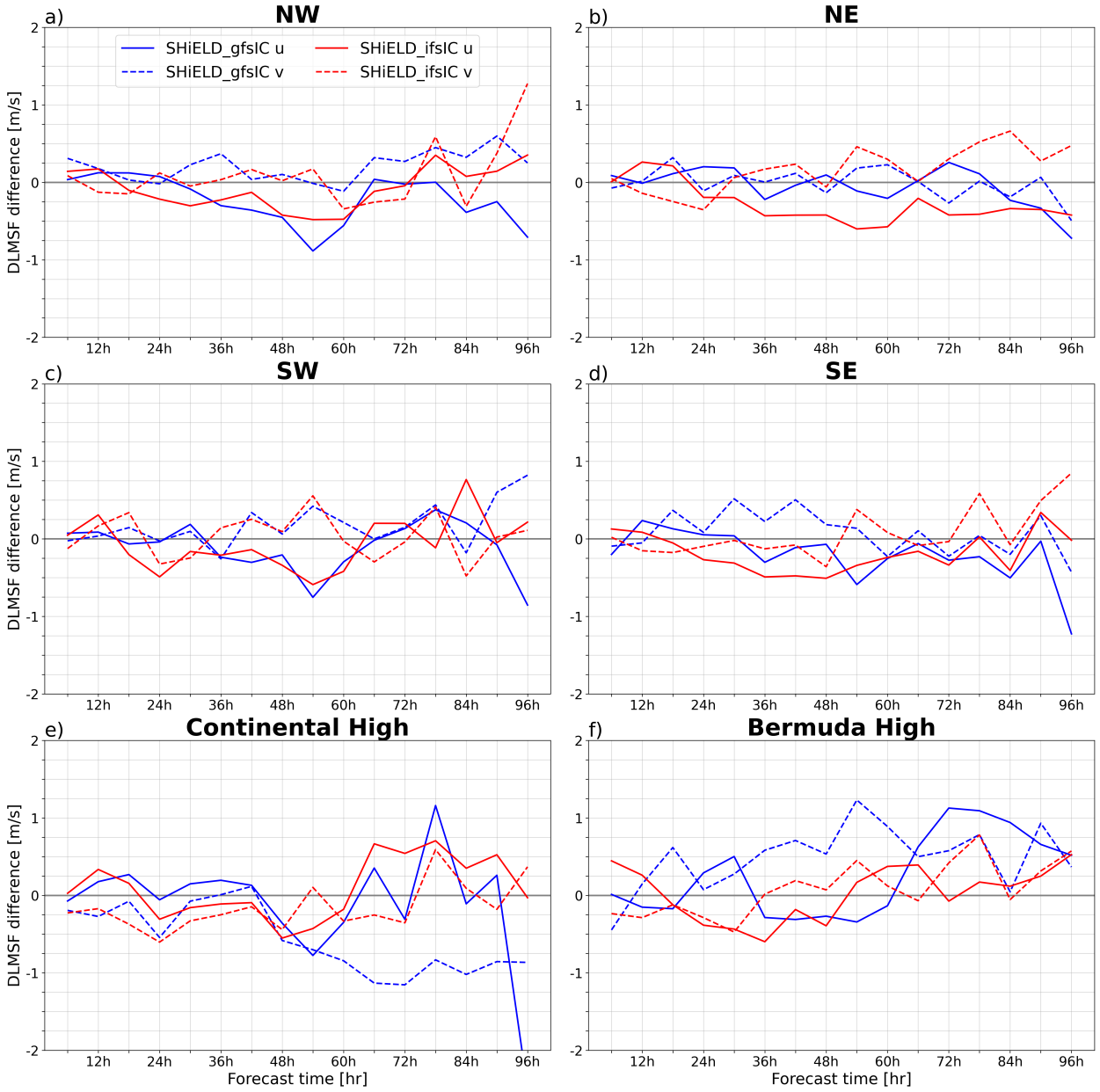

FIG. 3.8. As in Figure 3.4, but the blue lines show the SHiELD gfsIC and the red lines show the SHiELD ifsIC.

track forecasting challenge. Its track motion was governed mainly by the Bermuda High (Pasch et al. 2023).

A 5-day track forecast with 6-hourly forecast and BT positions was initialized on 17 September 2017 and is shown in Figure 3.9. The models ingesting GFS initial conditions show a northward track error at early lead times continuing through most of the forecast. The models initialized with IFS initial conditions follow a path similar to the BT. However, the IFS showed a southward track error beginning

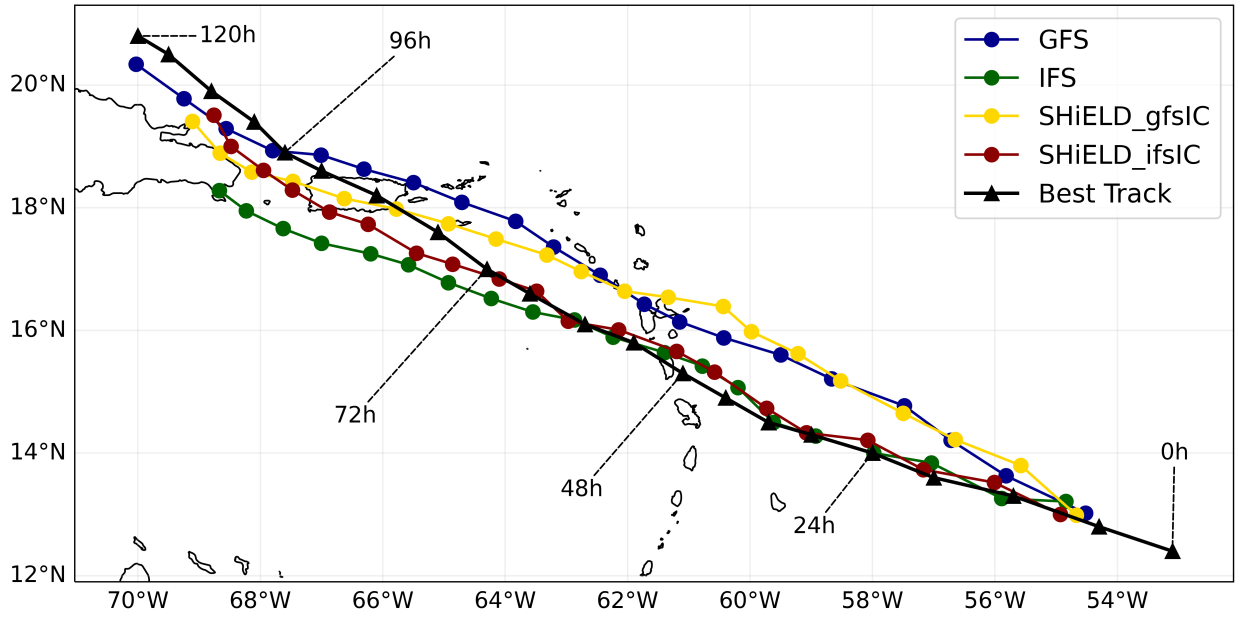

FIG. 3.9. As in Figure 3.1 but for Hurricane Maria. Tracks initialized on 17 September 2017 0Z.

around 48h, which causes the IFS to narrowly miss making landfall in Puerto Rico. Interestingly, the IFS showed a slow translation speed error around the same time as well. The southward track error in the IFS will be analyzed here.

An overview of the environmental, synoptic features is shown in Figure 3.10. The analysis fields show four main pressure systems of interest: a strong low pressure to the northwest (i.e., Hurricane Jose), high pressure to the north, a trough to the northeast, and the Bermuda High to the east. Maria is embedded within strong southeasterly winds imposed by the high pressure systems. The IFS forecast error (Fig. 3.10d) showed lower heights to the east and north, which imparts stronger southerly flow on Maria, and potentially explains its southward track error at 72h. Interestingly, a strong dipole of height differences to the northwest was due to differences in position and intensity of Hurricane Jose in the IFS versus the analysis field. The GFS forecast error (Fig. 3.10c) was relatively low, thus Maria's motion to the northwest in the GFS did not deviate very much. The model forecast difference is shown in Figure 3.10e, which shows that the IFS exhibited more easterly steering on Maria, reinforcing its southward track error.

Figure 3.11 quantifies the steering from the individual systems on Maria. This case is not as straightforward to interpret as the previous two. The IFS exhibits a southward track error at 72h, which is most likely caused by errors in the v-DLMSF. The Bermuda High, NW and SW quadrants show weaker positive v-DLMSF (e.g., weaker southerlies) in the IFS which supports its southward track error. However,

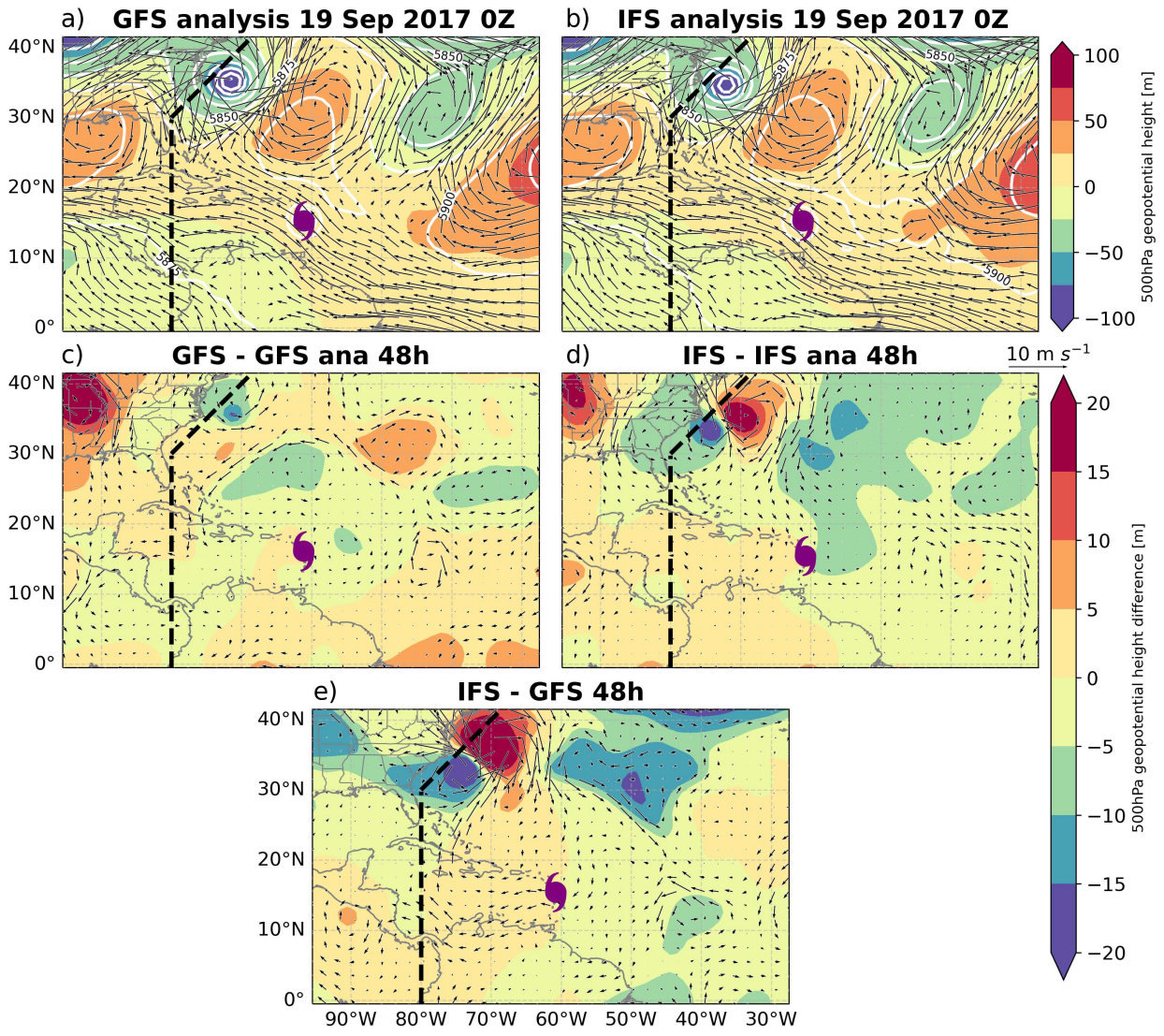

FIG. 3.10. As in Figure 3.2 but for Hurricane Maria at 48h.

the Continental High, and SE and NE quadrants also exhibit weaker negative v-DLMSF (e.g., weaker northerlies), which does not support the southward track error. A further look shows that the systems produce varying amounts of v-DLMSF with the strongest steering flow from the Bermuda High at 3-4 ms^{-1}, the Continental High and NE quadrant at 2-3 ms^{-1}, and smaller contributions of 1-2 ms^{-1} from the NW, SE, and SW quadrants. Southerly steering is produced by the NW and SW quadrants as well as the Bermuda High, while the NE and SE quadrants and Continental High contribute northerly steering flow on Maria. The sum contribution of errors from the northerly flows is slightly larger than the sum contributions of the southerly flow errors, resulting in a net southward track error.

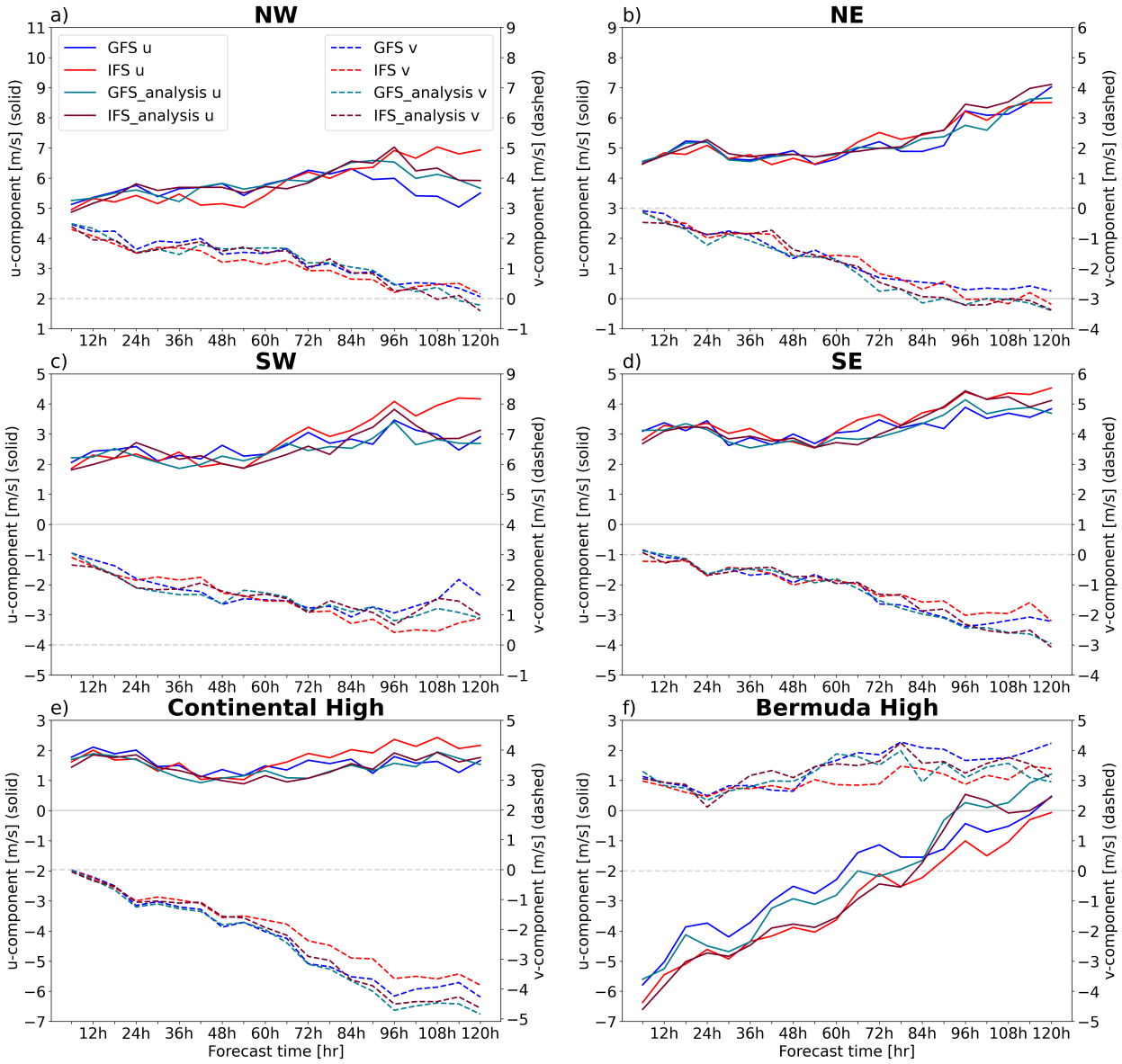

FIG. 3.11. As in Figure 3.3 but for Hurricane Maria.

Errors in the DLMSF are shown in Figure 3.12. Ultimately, the systems that produce weaker, southerly flow (e.g., Bermuda High, NW, SW) show more error, while the systems that produce weaker northerly flow (e.g., Continental High, SE, NE) show less error. As a result, the net steering on Maria was northerly, which produced the southward track error in the IFS. Recall that the IFS forecast showed large error from Hurricane Jose in Figure 3.10d. While large errors in the heights were evident to the northwest of Maria, the signal is not obvious in the DLMSF error. Because Hurricane Jose existed on the boundaries between the Bermuda High and Continental High, and NE and NW quadrants, the signal in the DLMSF error was distributed between them and is a caveat of our PV partitioning scheme.

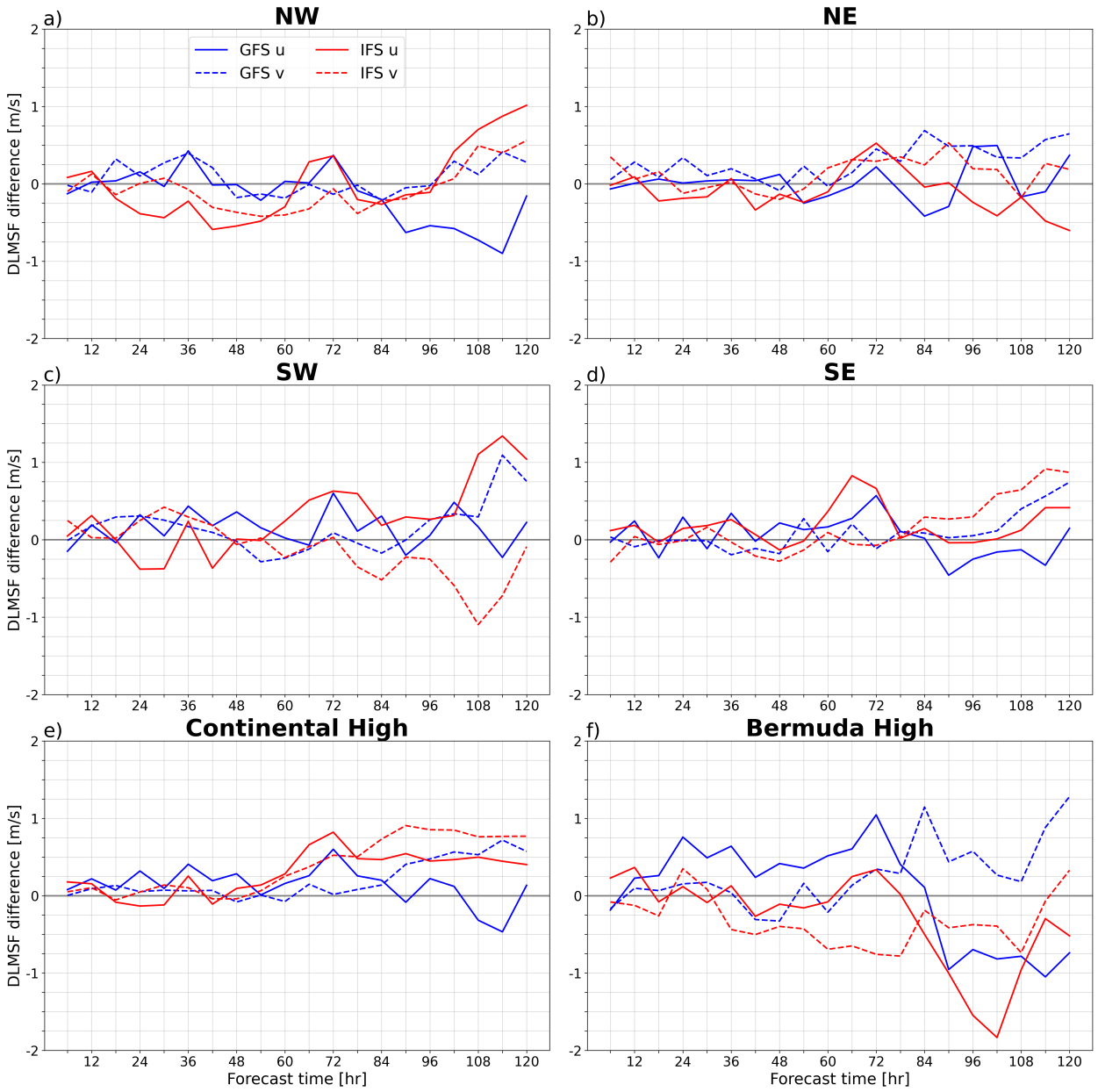

FIG. 3.12. As in Figure 3.4, but the blue lines show the GFS and the red lines show the IFS.

The GFS also showed a northward track error at 6h to around 72h. The northward track error should be caused by a stronger, positive v-DLMSF (e.g., stronger southerlies) and weaker, negative v-DLMSF (e.g., weaker northerlies). The Bermuda High, and NW and SW quadrants generally show stronger southerlies compared to the analysis DLMSF, with 0.25 ms^{-1} error contributed by each system as seen in Figure 3.12. The Continental High, and SE and NE quadrants also show weaker northerlies compared to the analysis DLMSF, with 0.25 ms^{-1} error contributed by each system. While these errors are small,

all systems produced a DLMSF error that helped steer Maria farther to the north, which produced its northward track error in the GFS.

CHAPTER 4

BASIN-SCALE ANALYSIS

4.1 DLMSF ERROR STATISTICS

The piecewise PV inversion tool was performed on 13 TCs during the 2017 North Atlantic hurricane season including Emily, Franklin, Gert, Harvey, Tropical Depression Ten, Irma, Jose, Katia, Lee, Maria, Nate, Ophelia, and Philippe. A common metric to quantify the amount of error in a prediction is the mean absolute error (MAE). The DLMSF MAE is calculated by summing the DLMSF error and dividing by the number of homogeneous cases at a certain lead time. Figure 4.1 quantifies the average DLMSF attributed to the different PV regions as a function of model and lead time. To a first order, the DLMSF MAE increases in time for all models and systems as expected. The Bermuda High contributes

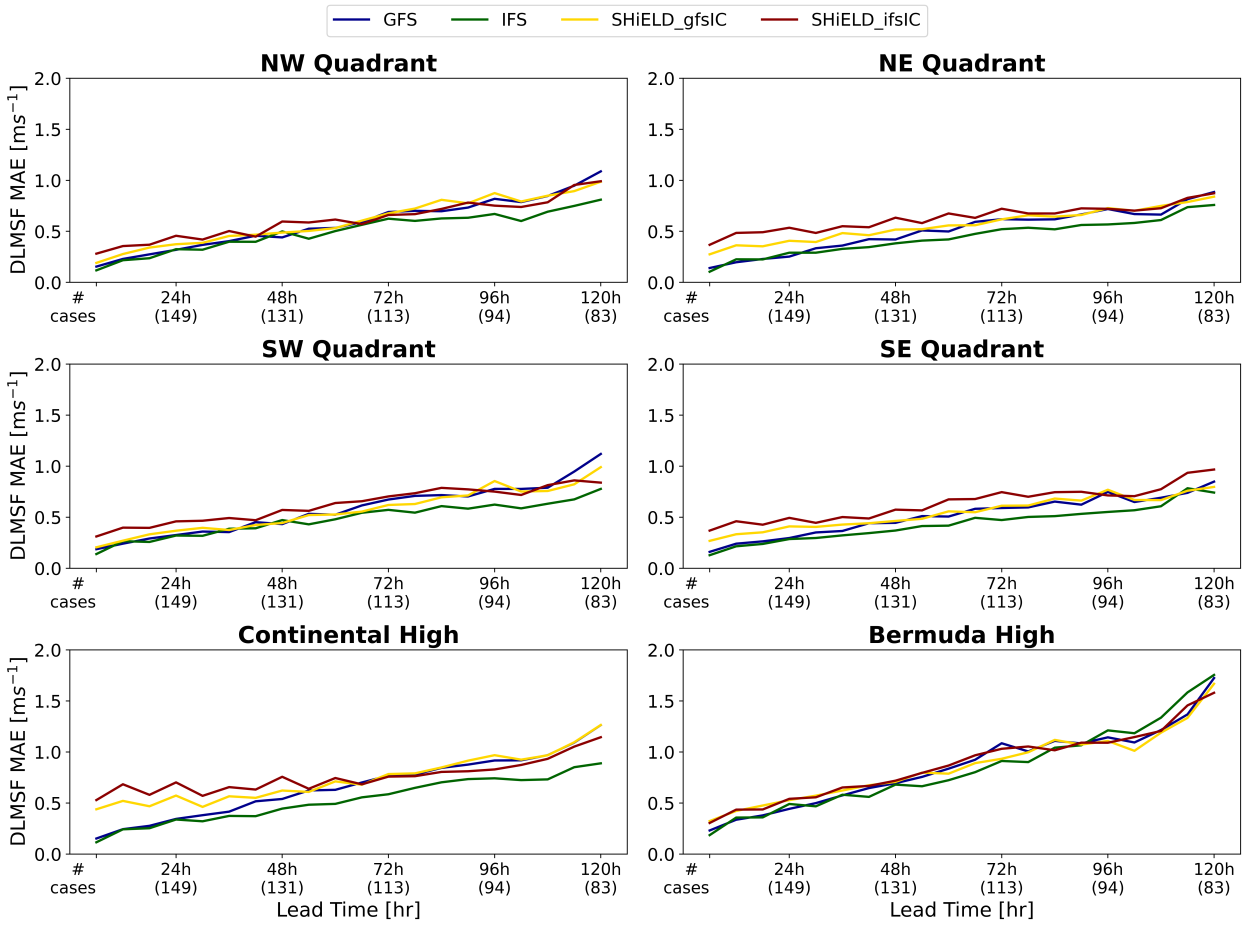

FIG. 4.1. Mean absolute error (MAE) of the DLMSF as a function of forecast hour. The number of cases shown along the x-axis are the homogeneous cases, that is, a case that is forecast in all models.

the largest DLMSF MAE, especially at later lead times. The Continental High produces a moderate amount of error, and the storm relative quadrants produce smaller errors. Generally, the DLMSF MAE is increasing slowly through 120h.

While the MAE describes the absolute average deviation of a measurement from the mean, it is important to also quantify the sign of the deviation (bias). Probability density functions (PDF) of the DLMSF error are plotted for each model as a function of system and lead time. Figure 4.2 shows the PDF plots for the GFS, Figure 4.3 for the IFS, Figure 4.4 for the SHiELD gfsIC, and Figure 4.5 for the SHiELD ifsIC. A positive bias indicates that forecast DLMSF was stronger than the observed (analysis) DLMSF while a negative bias indicates that forecast DLMSF was weaker than the observed DLMSF. In general for all models, all systems show a widening of the PDF with increasing lead time. The broadening indicates that errors increase with lead time. The broadening PDF is because model errors accrue and can cause larger errors at later lead times.

For the GFS, the PDF for the Bermuda High at 24h shows a relatively lower peak than the other systems which indicates the DLMSF errors are larger. The PDF also shows a slight positive bias indicating that the GFS predicts stronger DLMSF than the analysis. As the lead time increases, we see that the PDF has flattened out which shows errors in the DLMSF are increasing, and a slight positive bias continues. The Continental High shows a positive bias at all lead times meaning that the model predicts a consistently stronger DLMSF. The SE, SW, NW, and NE quadrants show a similar bias to the Continental High. Though the SE quadrant shows less DLMSF error compared with the other quadrants which have more error as shown by the broadening of the PDFs. For the IFS, the Bermuda High tells a similar story as in the GFS. These forecasts already display a moderate amount of error at 24h, and the errors grow tremendously with lead time compared to the other models. A slight negative bias in the Bermuda High at 24h is indicative of models predicting slightly lower DLMSF than the analysis. The Continental High, SE, SW, and NE quadrants show a positive bias at most if not all lead times. The NW quadrant shows a positive bias at early lead times that transition to a more-neutral bias at later lead times. The SHiELD gfsIC shows more DLMSF error from the Bermuda High than in the GFS and IFS. A strong positive bias in DLMSF is apparent at all lead times. In contrast, the Continental High seems to show less DLMSF error compared to the Bermuda High and quadrants. All quadrants show a positive bias at most lead times.

Another way to visualize the DLMSF error bias is in Figure 4.6 which shows plots of the mean DLMSF error as a function of system, lead time, and model. A positive mean (positive bias) indicates

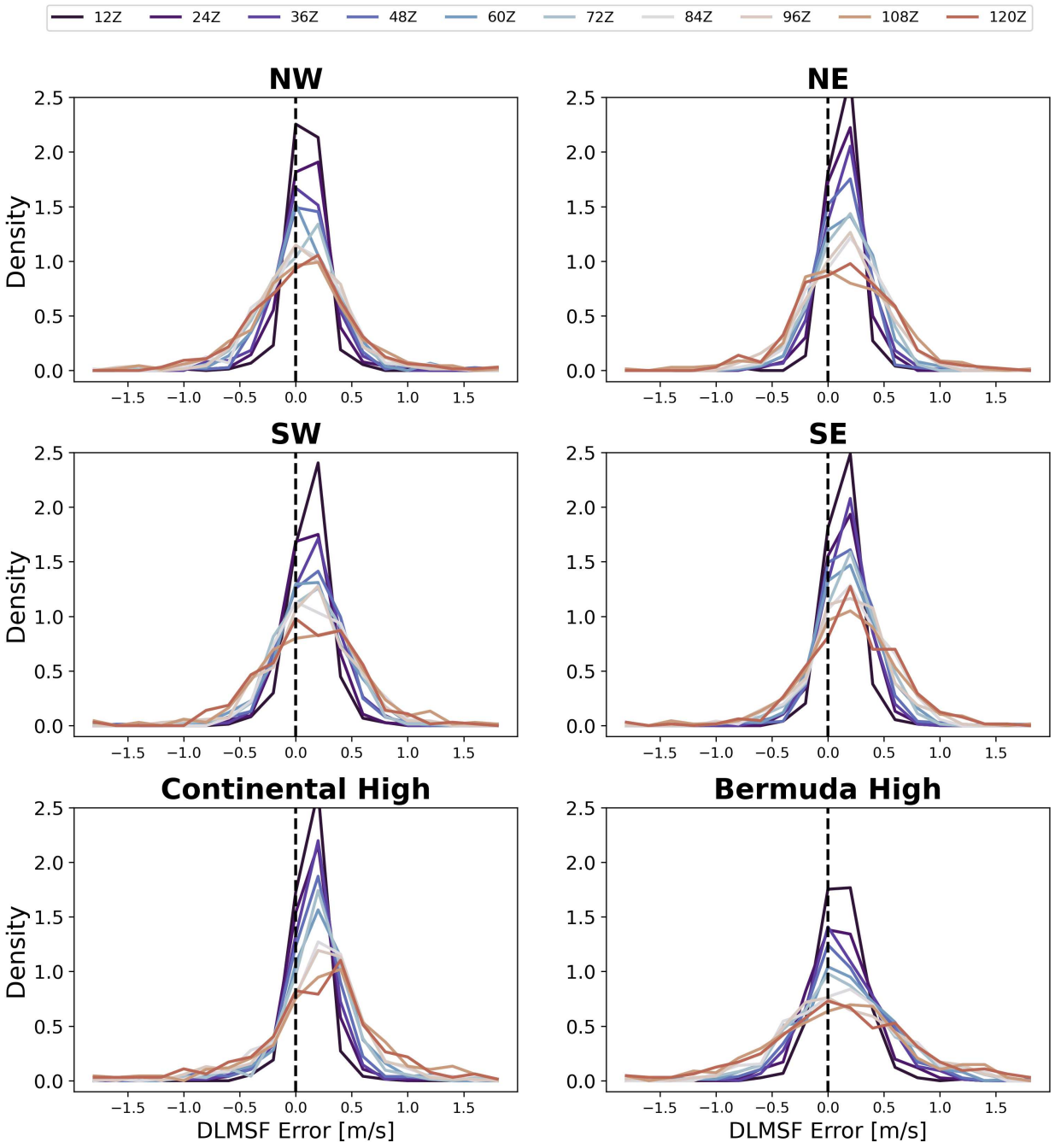

FIG. 4.2. Probability Density Functions (PDF) of DLMSF error as a function of system and forecast time for the GFS. The PDF was computed using all model forecast runs for an individual system at a certain lead time. The PDFs are plotted every 12 hours starting at 12 hours out to 5 days. Dark blue colors indicate early lead times and transition to warm red colors at later lead times. The same homogeneous cases used in Figure 4.1 are used for the PDFs.

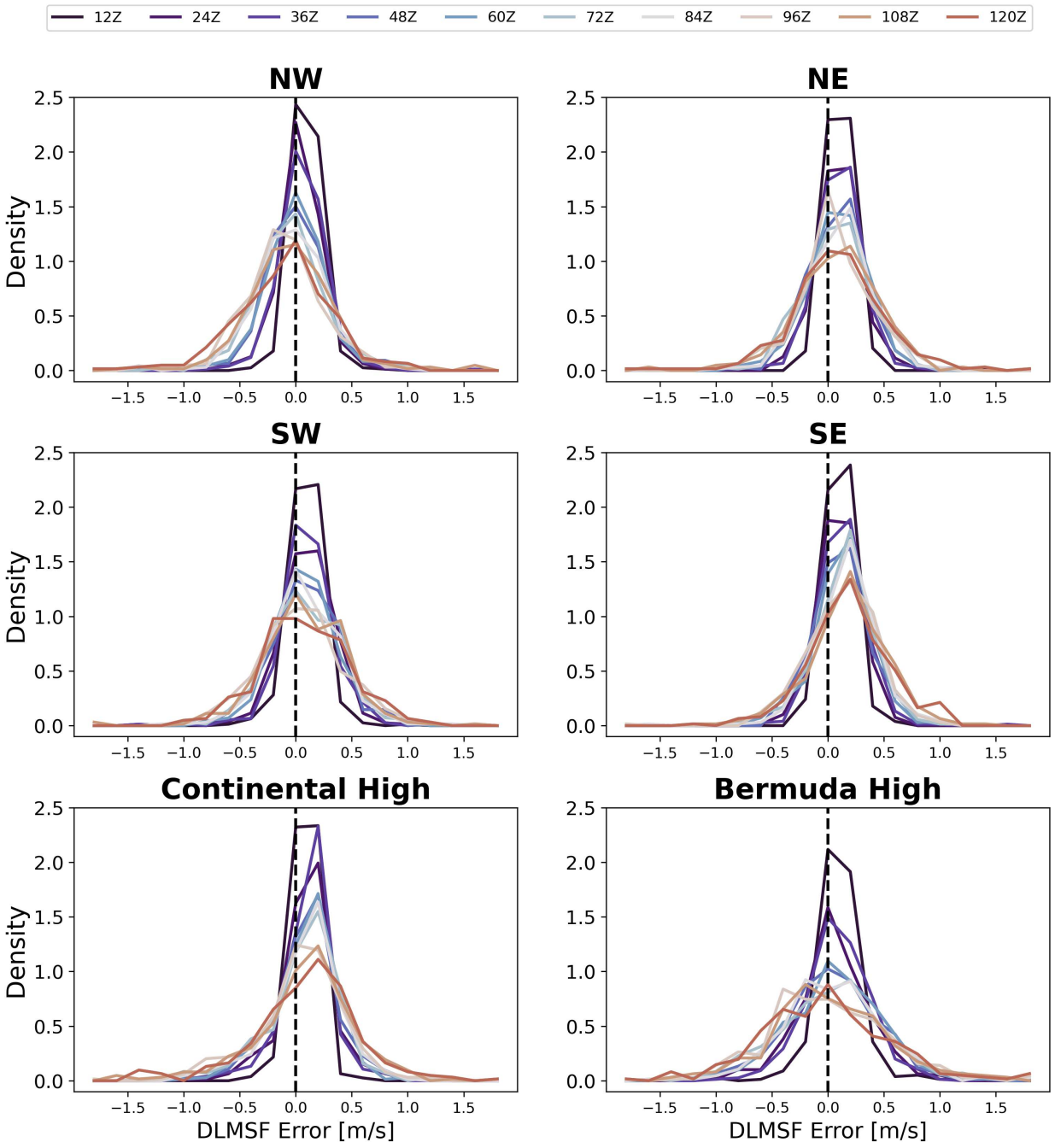

FIG. 4.3. As in Figure 4.2 but for the IFS.

that the forecasted DLMSF is stronger than the analysis, and a negative mean (negative bias) shows that the forecasted DLMSF is weaker than the analysis. When the mean is zero, this indicates that the DLMSF forecast errors are evenly distributed between positive and negative errors, resulting in a near neutral bias. The ±1 sigma bounds are also shaded for each model over the 5-day forecast. The largest biases are present in the Bermuda High, while moderate bias is shown in the Continental High, with

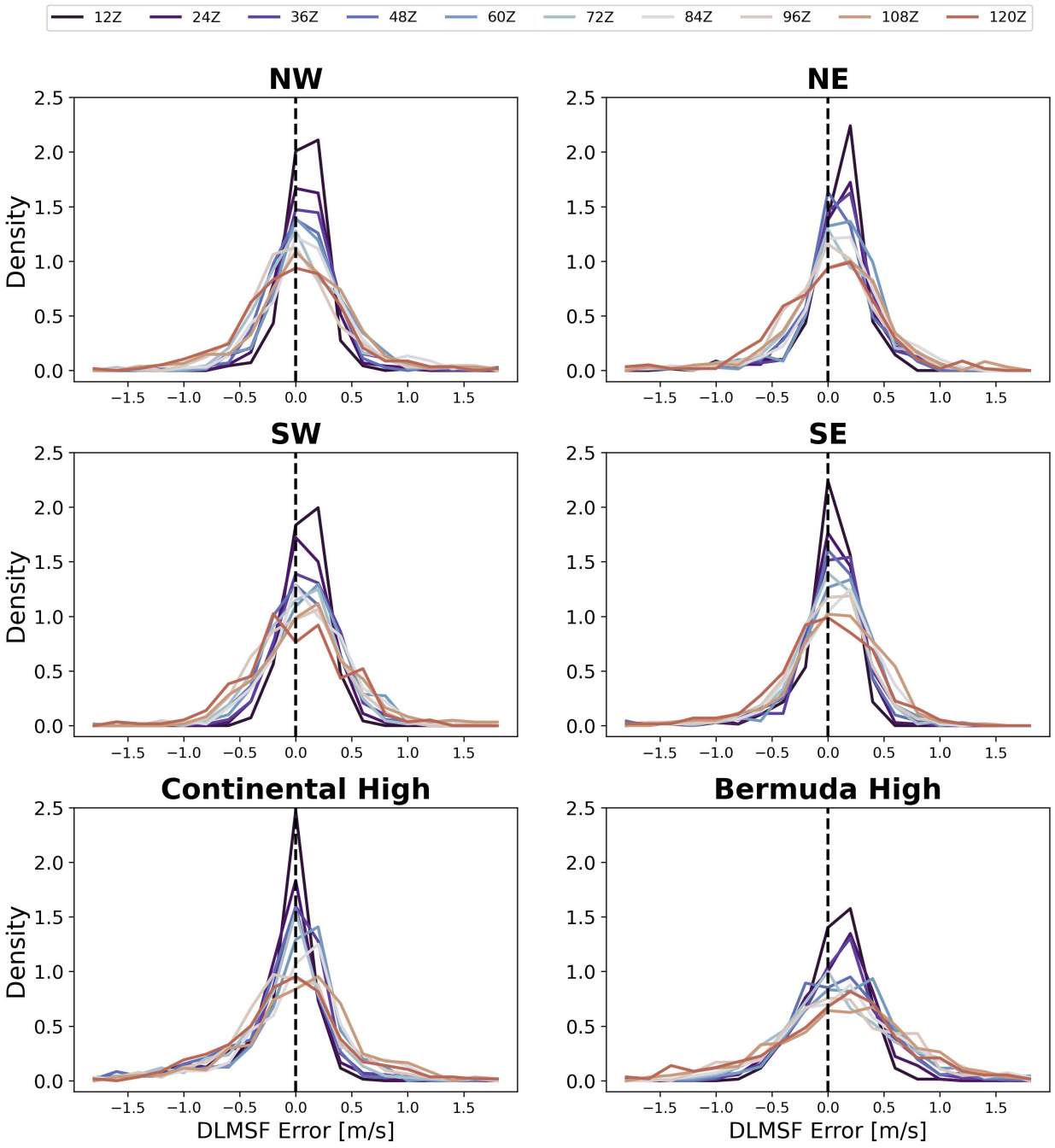

FIG. 4.4. As in Figure 4.2 but for the SHiELD gfsIC.

lower biases for the quadrants. For the Bermuda High, the SHiELD models generally produce a positive bias which mean the DLMSF from the Bermuda High is simulated too strongly. In contrast, the GFS and IFS show negative biases throughout the forecast. For the Continental High, the SHiELD models show a negative bias that transitions to a positive bias. The IFS shows a near neutral bias for most lead times, and the GFS bias is mainly positive. Similar biases for the models are shown in the SE quadrant. For the

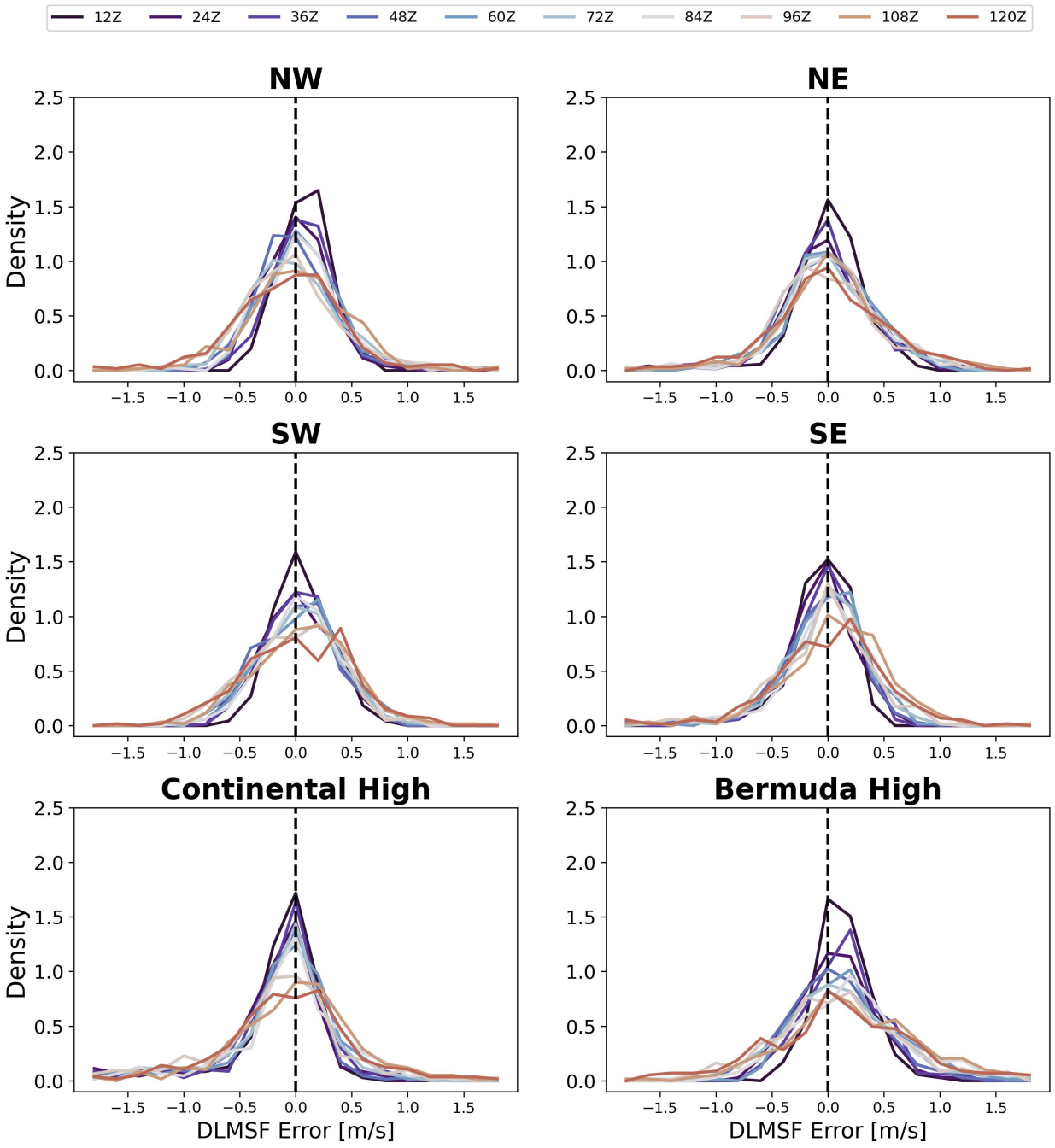

FIG. 4.5. As in Figure 4.2 but for the SHiELD ifsIC.

NW, NE, and SW quadrants, the mean is typically near zero at earlier lead times, indicating that there is little bias. A reason for the near zero bias for the quadrants is that the quadrants are storm-relative and the biases are averaged out.

The standard deviation of the DLMSF errors is plotted in Figure 4.7. The standard deviation is calculated similarly to the MAE, and both metrics illustrate the deviation of errors from the mean error.

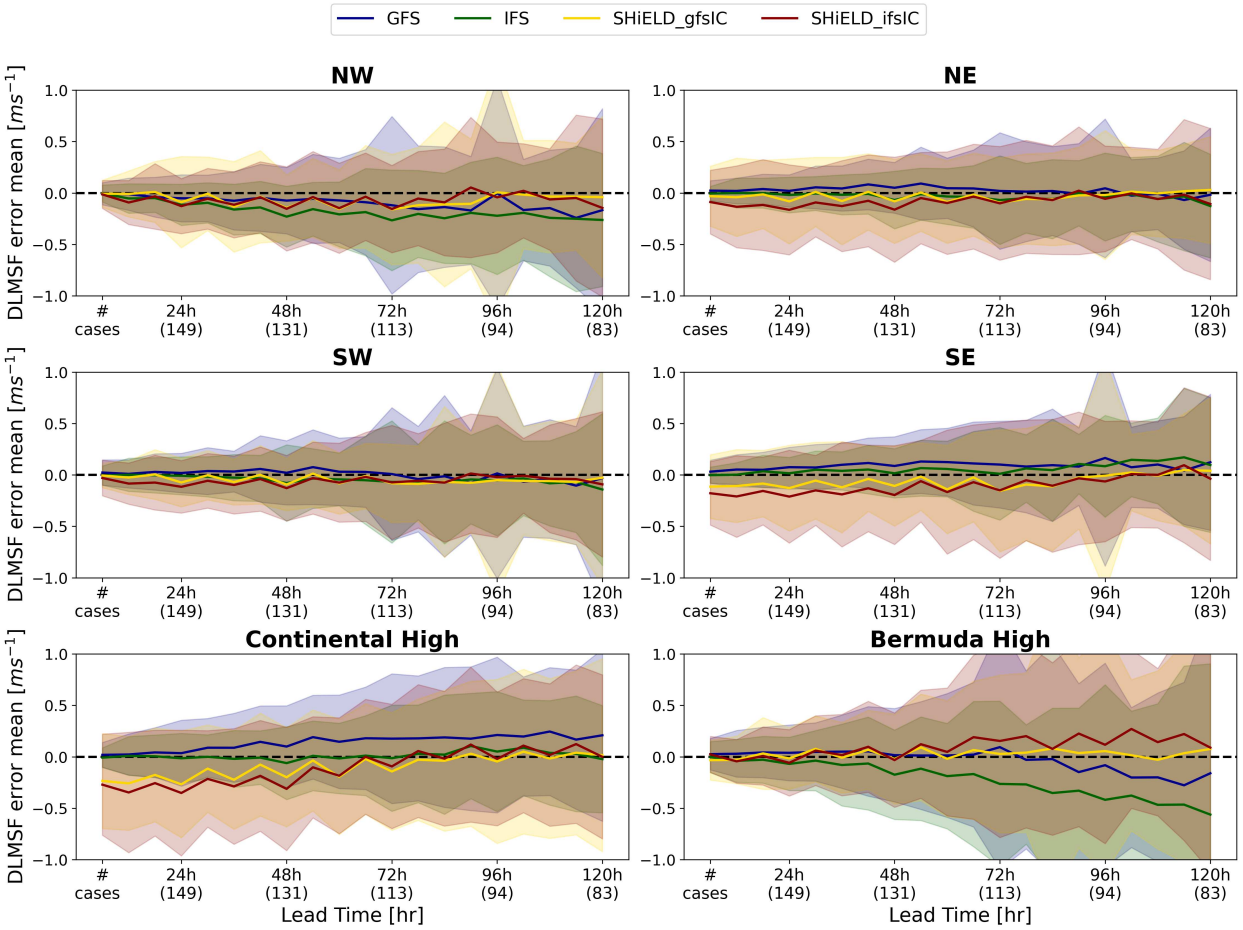

FIG. 4.6. The DLMSF error mean (bias) is plotted as a function of system and forecast time. The bias is plotted every 6 hours out to 5 days. The same homogeneous cases as in Figure 4.1 are used to plot the bias. The colored shading indicates the $\pm 1\sigma$ range of DLMSF errors that went into calculating the bias point for each model.

However, the standard deviation is the square root of the square of the errors compared to the absolute value of the error in the MAE, such that larger error differences are weighted more. Thus, standard deviation values are typically larger than MAE values. As expected, the standard deviation of the DLMSF errors follows very similarly to the MAE in 4.1.

4.2 COMPOSITE ANALYSES

As shown previously, the Bermuda High has the largest DLMSF MAE. This large MAE is more apparent at later lead times. To understand the result of the high DLMSF MAE, a composite analysis of the 500hPa balanced geopotential height solved from the Bermuda High PV perturbations is performed. Cases with DLMSF error greater than 0.75 standard deviation are composited for each model. 61 homogeneous cases are found to have a DLMSF error higher than 0.75 standard deviations at 24h for the

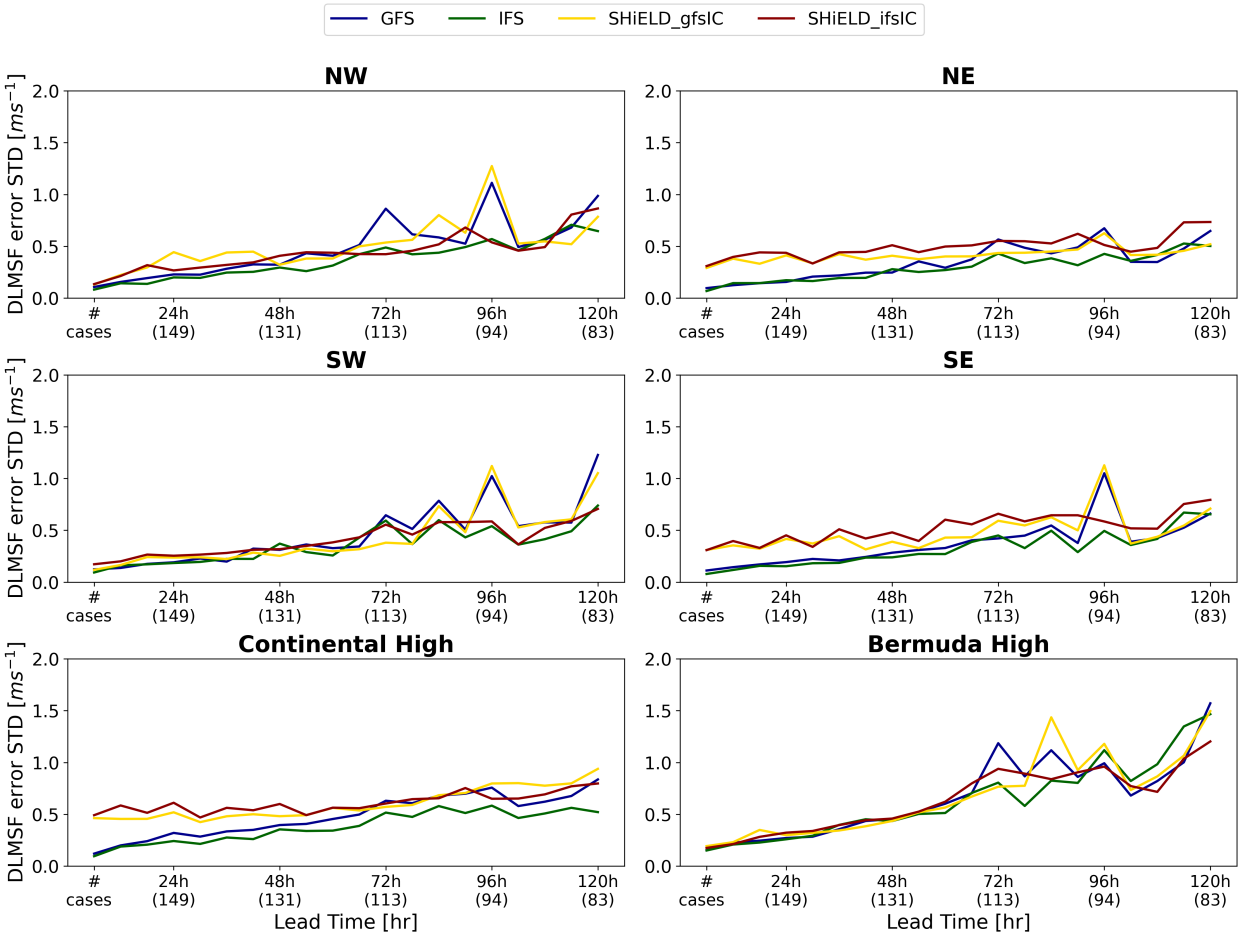

FIG. 4.7. The DLMSF error standard deviation for all storms is plotted. The standard deviation is plotted every 6 hours out to 5 days. The standard deviation is calculated using the same homogeneous cases as in Figure 4.1.

Bermuda High. The composite is shown in Figure 4.8. The contours show the average analysis balanced geopotential height field from the Bermuda High which can be thought of as the observed balanced mean field. The shading is the average error of the balanced geopotential height for these cases, or deviations from the observed balanced mean field. Storm locations for the 61 largest error cases are plotted as well. Figure 4.8b shows a weak bias in the geopotential height field of the western periphery of the Bermuda High in the IFS, which indicates that the strength of the Bermuda High is generally underrepresented at 24h. Colored markers illustrate hurricane locations following a recurving hurricane track pattern and is consistent with the track pattern associated with a weakened Bermuda High. The SHiELD ifsIC in Figure 4.8d shows a similar weak bias in the geopotential height field, but the spatial extent of the height errors is spread farther east and is not so centered on the western periphery. The GFS in Figure 4.8a the SHiELD gfsIC in Figure 4.8c show broad areas of weak bias in the geopotential

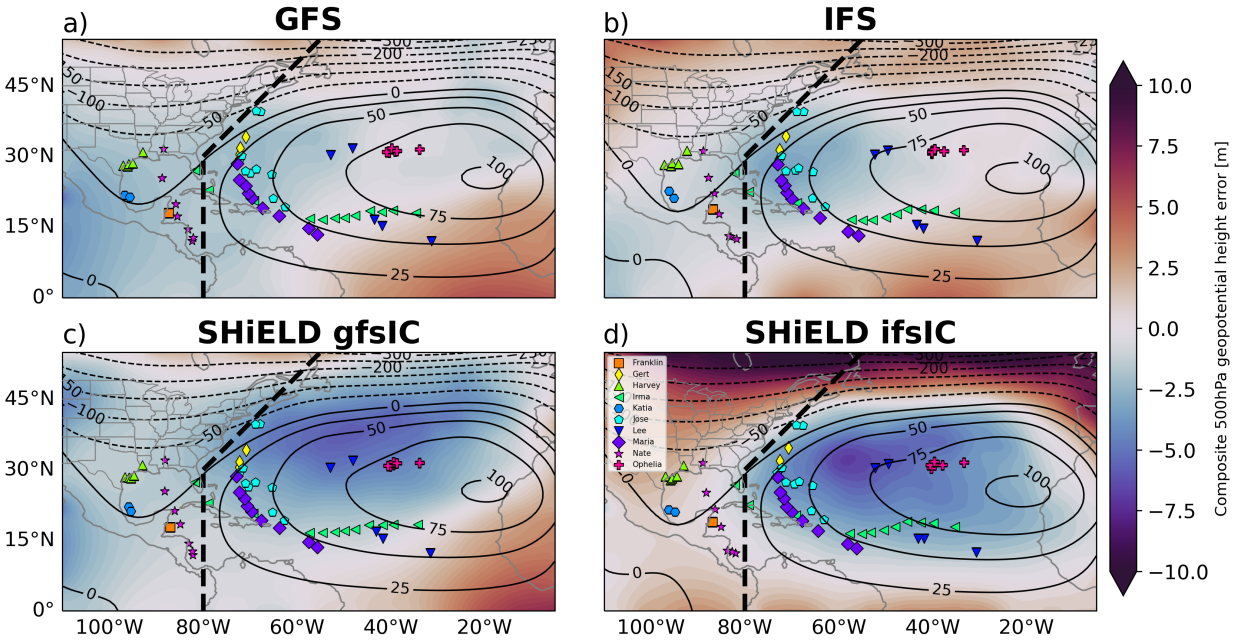

FIG. 4.8. Composite analysis of balanced geopotential height analysis field (contours, m) and balanced geopotential height error (shading, m) for 61 homogeneous cases exceeding 0.75 standard deviations of DLMSF for the Bermuda High at 24h. The 61 cases are plotted, with markers denoting the storm's positions (markers).

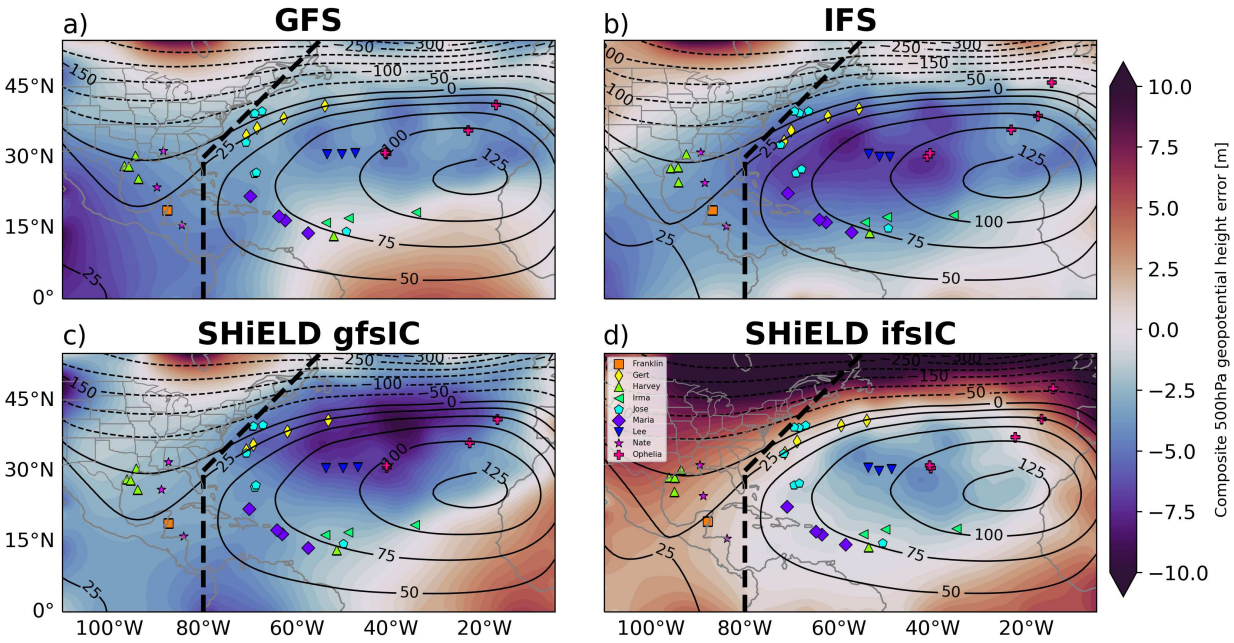

FIG. 4.9. As in Figure 4.8, but for 48h. 35 homogeneous cases are displayed.

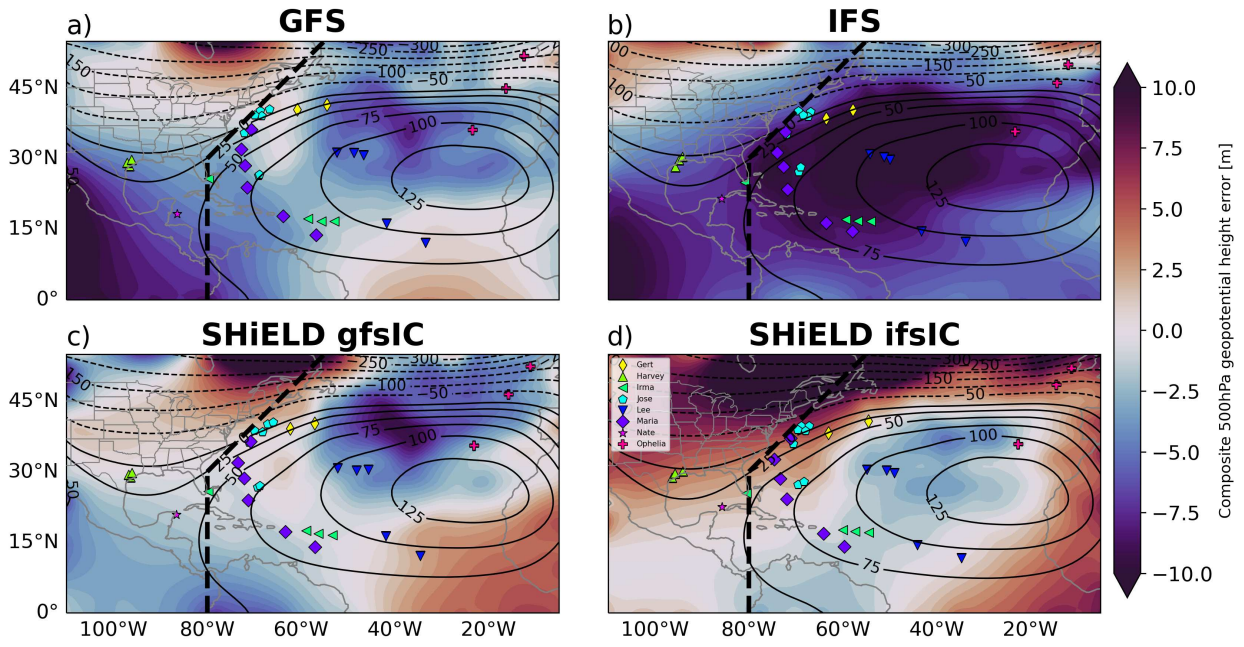

FIG. 4.10. As in Figure 4.8, but for 72h. 31 homogeneous cases are displayed.

height field in the domain but these errors are not consistent with a weakened Bermuda High as is in the IFS.

Chen et al. (2019) calculated the track error in forecasts runs of Hurricane Irma and Hurricane Maria in the GFS, IFS, SHiELD gfsIC, and SHiELD ifsIC. The average total track error over all the forecasts for each storm was decomposed into an along-track error which is associated with the TC translation speed and a cross-track error component which is related to the TC directional changes. The IFS showed that the along-track error was consistently a signification fraction of the total track error, whereas the along-track and cross-track errors were more evenly split in the SHiELD ifsIC for both storms. In conclusion, they found the along-track error showed a strong negative bias over all forecast times meaning that the translation speed was consistently weaker in the IFS forecast compared to the verified track. The findings in this thesis support the conclusion of Chen et al. (2019), where the slow translation speed bias in the IFS is caused by an underrepresented Bermuda High in IFS forecasts which produces weaker anticyclonic steering on TCs.

The same composite analysis is done for 48h (Fig. 4.9). Similar spatial patterns in the balanced geopotential height error are observed in the 48h composite as in 24h composite. Moreover, there is noticeably larger error in all of the models which is expected given that errors tend to accumulate and grow with time. However, the SHiELD ifsIC at 48h shows lower balanced geopotential height error in the

central region of the Bermuda High and near-zero error in the western periphery of the Bermuda High. The SHiELD ifsIC also shows larger errors in the mid-latitudes. Figure 4.10 shows the composite at 72h. Larger errors are observed at 72h compared to the earlier forecast times. Notably, the magnitudes of the errors are higher, but the spatial patterns of the errors are different. The higher errors at 72h suggests that the differences in the models at longer lead times are less related to the initial conditions, and that the model dynamics and/or physics are starting to play a larger role in producing errors.

CHAPTER 5

DISCUSSION AND CONCLUSIONS

We utilize the piecewise PV inversion diagnostic technique to identify the sources of errors in TC track forecasts. Specifically, the contribution of steering from individual large-scale pressure systems and errors in the steering is quantified. While several previous studies have used the piecewise PV inversion diagnostic tool in case studies of individual storms, this study is the first to use piecewise PV inversion systematically on an entire hurricane season to investigate errors that occur consistently in time, or model biases.

To perform piecewise PV inversion systematically on an entire hurricane season, the PV framework in Wu et al. (2003) was adopted and altered for our objective. The perturbation PV was isolated by removing the basic PV to quantify only the influence of the large-scale environment on TC movement. The PV perturbation field was subjectively partitioned in six regions geographically by sign: the Bermuda High, Continental High, and four low quadrants of the TC. The nonlinear balanced flow was inverted from each PV perturbation piece separately to break down the environmental wind into its core components. The Deep Layer Mean Steering Flow (DLMSF) metric was calculated to quantify the steering from these individual pressure systems on TC movement. DLMSF errors were computed by comparing the forecast to analysis fields. Lead-lag correlation analyses between DLMSF errors and track errors showed a maximum correlation from -24 to 0 hours, meaning track errors were caused by errors in the TC DLMSF up to 24 hours before. The correlations were moderate meaning DLMSF is a sufficient proxy for TC movement and that DLMSF errors are representative of TC movement errors in model forecasts.

An in-depth analysis of steering flow from forecasts of three hurricanes: Harvey, Irma, and Maria is performed. The piecewise PV inversion is used to diagnose the contributors of forecast track error to steering flow errors. Harvey's weak steering environment was caused by two anticyclones contributing opposing flow, which ultimately led to its stall. The GFS exhibited a strong southwest track error attributed to errors in the u-DLMSF which favored westward advection. Irma displayed a drastic northward track error in the SHiELD gfsIC compared to the SHiELD ifsIC and BT, which placed its landfalling location near Miami as opposed to southwest Florida. The diagnosis showed that this error was mainly caused by error in the DLMSF from two opposing anticyclonic circulations, which imparted opposing

v-DLMSF steering, but an overall net southerly steering on Irma. Maria's track in the IFS was characterized by a southward track error, which resulted in the hurricane not actually making landfall in Puerto Rico. The DLMSF diagnosis showed opposing northerly and southerly steering on Maria from various systems, but net larger northerly steering error resulted in Maria's southward track error. Large errors from Hurricane Jose to the northwest of Maria likely also played a part in the steering. Yet, the impact of error in Jose on Maria's movement was difficult to interpret because Jose existed on the boundary between the Continental High and Bermuda High and the DLMSF error attributed to Jose was split.

A basin-scale analysis of thirteen storms was performed to ascertain any model biases. The DLMSF Mean Absolute Error (MAE) was calculated for all PV systems and showed that the Bermuda High produced the largest errors, the Continental High produced moderate errors, and the four quadrants each produced lower errors. To understand why the Bermuda High produced the most DLMSF MAE, cases with error more than 0.75 standard deviations associated with the Bermuda High were composited at 24-, 48-, and 72-hrs forecast times. The composite results showed lower balanced geopotential heights around the western side of the Bermuda High for all lead times and models, meaning the models consistently underrepresented the strength of the Bermuda High in erroneous forecasts. The storm locations for the high error cases were also plotted and showed a tendency for TCs to recurve, which is consistent with observed storm movement in the presence of a weaker Bermuda High in the North Atlantic.

Piecewise PV inversion was performed on the 2017 North Atlantic hurricane season in this study. While it would be ideal to have multiple years of data for analysis, the 2017 North Atlantic season provides more than 100 cases at short lead times, which provides an essential proof of concept for using this diagnostic technique for assessing model biases in track error. Future work should include extending this analysis to multiple years to include a larger sample size as well as other ocean basins, although the issue of model consistency across multiple seasons then becomes an issue.

The choice of PV perturbation partitioning scheme is dependent on the atmospheric feature that is being analyzed. We required a method to systematically analyze the track errors for multiple storms, and devised the current partitioning scheme. However, some limitations exist with the current partitioning scheme. As was shown in the case study of Hurricane Maria, errors in the representation of Hurricane Jose to Maria's northwest existed on the boundary separating the PV regions. Consequently, the DLMSF error from the misrepresentation of Hurricane Jose to was not obvious to interpret and the

inability to identify the influence on a TC from an individual PV system in time is a caveat of the current partitioning scheme. A more complex algorithm would be required to analyze the contribution from individual systems. Still, the current partitioning method provides a first step towards a general partitioning scheme.

Our analysis only allows for TC movement from advection, but as we know in the real atmosphere, a TC's intensity may also contribute to its own movement through a two-way interaction with its environment, known as the Beta effect (Marks 1992). The Shapiro decomposition removes the intensity aspect by removing the basic PV field from the perturbation field, and only the perturbation field is used to quantify the DLMSF. Any feedback between the intensity and movement are thus eliminated, and the advection of TCs by their environmental steering can be looked at as a one-way interaction.

Another possible limitation of our analysis is that the 925-300 hPa layer-mean is used to calculate the DLMSF, however the instantaneous height of the TC vortex could be important in determining which atmospheric layers contribute to its movement. While the 925-300hPa levels span most vortex heights, not all TC vortices (i.e, weak TCs) span the entire height of the column (DesRosiers et al. 2023). For a shallow vortex in the real atmosphere, the steering levels above the height of the vortex should not have a large impact on TC motion. However, the DLMSF does not account for varying vortex height and may over-contribute steering from atmospheric layers when the vortex is weak, which may cause the DLMSF to not accurately predict TC motion at times. A more accurate representation of the steering flow may be calculated by incorporating vortex height into the steering flow calculation. However, the lead-lag correlation analysis in Section 2.3 showed moderate correlations between DLMSF error and track error, and thus the DLMSF from 925-300hPa is a reasonable proxy for TC motion.

In this research, the influence of TC PV is removed by taking the axisymmetric wind field in a circle with a radius of 2000 km around the TC center. Subsequently, the basic stream function, geopotential height, and PV fields can be calculated. While 2000 km is a reasonable radius to capture most of the cyclone's flow, this constant radius may not be the most optimal radius for all storms. In the case of a TC with a structure that exists outside of this radius, the basic field will not be fully captured, leading to an excess of the basic field being incorporated into the perturbation field, which may cause errors in the DLMSF. Most TCs, however, are smaller than the 2000 km radius, and the cyclone circulation will be overestimated. As a result, some of the perturbation field around the cyclone may be excluded, which may affect the DLMSF.

This research has shown that the piecewise PV inversion inversion technique is a practical diagnostic tool in understanding track errors in TCs. The work presented here can be extended by developing a specific PV perturbation partitioning scheme to look at specific geographic model biases, or a more complex partitioning scheme to identify the contribution to DLMSF error from individual PV systems. Other future work can include the addition of more seasons and different numerical weather prediction models. It may also be interesting to apply this methodology to different ocean basins, such as the western North Pacific, where different synoptic steering systems exist such as the Meiyu front. While track forecasts have improved substantially, large track errors still exist, and the identification of model biases is essential to improve track error. Even small track errors can result in impacts in vastly different regional impacts. For example, in 2022, 48 hours prior to landfall, Hurricane Ian's most likely forecast track was a landfall in Tampa Bay, Florida; However, minimal forecast error resulted in a landfall further south, and Tampa Bay escaped the worst impacts from Ian. In conclusion, the identification of model biases is the first step in correcting them. The work presented here will contribute to reducing both large and small track errors in the future through the identification of model biases.

REFERENCES

Baxter, M. A., P. N. Schumacher, and J. M. Boustead, 2011: The use of potential vorticity inversion to evaluate the effect of precipitation on downstream mesoscale processes. *Quarterly Journal of the Royal Meteorological Society*, **137 (654)**, 179–198.

Blake, E. S. and D. A. Zelinsky, 2018: National hurricane center tropical cyclone report hurricane harvey. 77, URL https://www.nhc.noaa.gov/data/tcr/AL092017_Harvey.pdf.

Cangialosi, J. P., A. S. Latto, and R. Berg, 2021: National hurricane center tropical cyclone report hurricane irma. 111, URL https://www.nhc.noaa.gov/data/tcr/AL112017_Irma.pdf.

Chan, J. C. L. and W. M. Gray, 1982: Tropical cyclone movement and surrounding flow relationships. *Monthly Weather Review*, **110 (10)**, 1354 – 1374, doi: https://doi.org/10.1175/1520-0493(1982)110<1354:TCMASF>2.0.CO;2, URL https://journals.ametsoc.org/view/journals/mwre/110/10/1520-0493_1982_110_1354_tcmasf_2_0_co_2.xml.

Charney, J., 1955: The use of the primitive equations of motion in numerical prediction. *Tellus*, **7 (1)**, 22–26, doi: 10.3402/tellusa.v7i1.8772, URL https://doi.org/10.3402/tellusa.v7i1.8772, https://doi.org/10.3402/tellusa.v7i1.8772.

Chen, G. T.-J., C.-C. Wang, and S. C.-S. Liu, 2003: Potential vorticity diagnostics of a mei-yu front case. *Monthly Weather Review*, **131 (11)**, 2680 – 2696, doi: https://doi.org/10.1175/1520-0493(2003)131<2680:PVDOAM>2.0.CO;2, URL https://journals.ametsoc.org/view/journals/mwre/131/11/1520-0493_2003_131_2680_pvdoam_2.0.co_2.xml.

Chen, J.-H., X. Chen, S.-J. Lin, L. Magnusson, M. Bender, L. Zhou, and S. Rees, 2018: Tropical cyclones in gfdl fvgfs—impacts of dycore, physics and initial conditions. *33rd Conf. on Hurricane and Tropical Meteorology*.

Chen, J.-H., et al., 2019: Advancements in hurricane prediction with noaa's next-generation forecast system. *Geophysical Research Letters*, **46 (8)**, 4495–4501.

Davis, C. A., 1992a: Piecewise potential vorticity inversion. *Journal of Atmospheric Sciences*, **49 (16)**, 1397 – 1411, doi: https://doi.org/10.1175/1520-0469(1992)049<1397:PPVI>2.0.CO;2, URL https://journals.ametsoc.org/view/journals/atsc/49/16/1520-0469_1992_049_1397_ppvi_2_0_co_2.xml.

Davis, C. A., 1992b: A potential-vorticity diagnosis of the importance of initial structure and condensational heating in observed extratropical cyclogenesis. *Monthly Weather Review*, **120 (11)**,

2409 – 2428, doi: https://doi.org/10.1175/1520-0493(1992)120<2409:APVDOT>2.0.CO;2, URL https://journals.ametsoc.org/view/journals/mwre/120/11/1520-0493_1992_120_2409_apvdot_2_0_co_2.xml.

Davis, C. A. and K. A. Emanuel, 1991: Potential vorticity diagnostics of cyclogenesis. *Monthly Weather Review*, **119 (8)**, 1929 – 1953, doi: https://doi.org/10.1175/1520-0493(1991)119<1929:PVDOC>2.0.CO;2, URL https://journals.ametsoc.org/view/journals/mwre/119/8/1520-0493_1991_119_1929_pvdoc_2_0_co_2.xml.

DeHart, J. C. and M. M. Bell, 2020: A comparison of the polarimetric radar characteristics of heavy rainfall from hurricanes harvey (2017) and florence (2018). *Journal of Geophysical Research: Atmospheres*, **125 (11)**, e2019JD032 212, doi: https://doi.org/10.1029/2019JD032212, URL https://agupubs.onlinelibrary.wiley.com/doi/abs/10.1029/2019JD032212, e2019JD032212 10.1029/2019JD032212, https://agupubs.onlinelibrary.wiley.com/doi/pdf/10.1029/2019JD032212.

DesRosiers, A. J., M. M. Bell, P. J. Klotzbach, M. S. Fischer, and P. D. Reasor, 2023: Observed relationships between tropical cyclone vortex height, intensity, and intensification rate. *Geophysical Research Letters*, **50 (8)**, e2022GL101 877, doi: https://doi.org/10.1029/2022GL101877, URL https://agupubs.onlinelibrary.wiley.com/doi/abs/10.1029/2022GL101877, e2022GL101877 2022GL101877, https://agupubs.onlinelibrary.wiley.com/doi/pdf/10.1029/2022GL101877.

ECMWF, 2016: Ifs documentation cy41r2 - technical report. ECMWF, URL https://www.ecmwf.int/node/16646, doi: 10.21957/9phrx9eu.

Ertel, H., 1942: Ein neuer hydrofynamischer wirbelsatz. *Meteor. Z.*, **59**, 277–282.

Franklin, J. L., S. E. Feuer, J. Kaplan, and S. D. Aberson, 1996: Tropical cyclone motion and surrounding flow relationships: Searching for beta gyres in omega dropwindsonde datasets. *Monthly Weather Review*, **124 (1)**, 64 – 84, doi: https://doi.org/10.1175/1520-0493(1996)124<0064:TCMASF>2.0.CO;2, URL https://journals.ametsoc.org/view/journals/mwre/124/1/1520-0493_1996_124_0064_tcmasf_2_0_co_2.xml.

Fujiwhara, S., 1921: The natural tendency towards symmetry of motion and its application as a principle in meteorology. *Quarterly Journal of the Royal Meteorological Society*, **47 (200)**, 287–292, doi: https://doi.org/10.1002/qj.49704720010, URL https://rmets.onlinelibrary.wiley.com/doi/abs/10.1002/qj.49704720010, https://rmets.onlinelibrary.wiley.com/doi/pdf/10.1002/qj.49704720010.

Gray, W. M., 1998: The formation of tropical cyclones. *Meteorology and atmospheric physics*, **67 (1-4)**, 37–69.

Hakim, G. J., D. Keyser, and L. F. Bosart, 1996: The ohio valley wave-merger cyclogenesis event of 25–26 january 1978. part ii: Diagnosis using quasigeostrophic potential vorticity inversion. *Monthly Weather Review*, **124 (10)**, 2176 – 2205, doi: https://doi.org/10.1175/1520-0493(1996)124<2176:TOVWMC>2.0.CO;2, URL https://journals.ametsoc.org/view/journals/mwre/124/10/1520-0493_1996_124_2176_tovwmc_2_0_co_2.xml.

Harris, L., et al., 2020: Gfdl shield: A unified system for weather-to-seasonal prediction. *Journal of Advances in Modeling Earth Systems*, **12 (10)**, e2020MS002 223.

Hoskins, B. J., M. E. McIntyre, and A. W. Robertson, 1985: On the use and significance of isentropic potential vorticity maps. *Quarterly Journal of the Royal Meteorological Society*, **111 (470)**, 877–946.

Huo, Z., D.-L. Zhang, and J. R. Gyakum, 1999: Interaction of potential vorticity anomalies in extratropical cyclogenesis. part i: Static piecewise inversion. *Monthly Weather Review*, **127 (11)**, 2546 – 2562, doi: https://doi.org/10.1175/1520-0493(1999)127<2546:IOPVAI>2.0.CO;2, URL https://journals.ametsoc.org/view/journals/mwre/127/11/1520-0493_1999_127_2546_iopvai_2.0.co_2.xml.

Klotzbach, P. J., C. J. S. III, J. M. Collins, M. M. Bell, E. S. Blake, and D. Roache, 2018: The extremely active 2017 north atlantic hurricane season. *Monthly Weather Review*, **146 (10)**, 3425 – 3443, doi: https://doi.org/10.1175/MWR-D-18-0078.1, URL https://journals.ametsoc.org/view/journals/mwre/146/10/mwr-d-18-0078.1.xml.

Korner, S. O. and J. E. Martin, 2000: Piecewise frontogenesis from a potential vorticity perspective: Methodology and a case study. *Monthly Weather Review*, **128 (5)**, 1266 – 1288, doi: https://doi.org/10.1175/1520-0493(2000)128<1266:PFFAPV>2.0.CO;2, URL https://journals.ametsoc.org/view/journals/mwre/128/5/1520-0493_2000_128_1266_pffapv_2.0.co_2.xml.

Lackmann, G. M., 2002: Cold-frontal potential vorticity maxima, the low-level jet, and moisture transport in extratropical cyclones. *Monthly Weather Review*, **130 (1)**, 59 – 74, doi: https://doi.org/10.1175/1520-0493(2002)130<0059:CFPVMT>2.0.CO;2, URL https://journals.ametsoc.org/view/journals/mwre/130/1/1520-0493_2002_130_0059_cfpvmt_2.0.co_2.xml.

Landsea, C. W. and J. P. Cangialosi, 2018: Have we reached the limits of predictability for tropical cyclone track forecasting? *Bulletin of the American Meteorological Society*, **99 (11)**, 2237 – 2243, doi: https://doi.org/10.1175/BAMS-D-17-0136.1, URL https://journals.ametsoc.org/view/journals/bams/99/11/bams-d-17-0136.1.xml.

Marks, D. G., 1992: The beta and advection model for hurricane track forecasting.

Miller, R. J., A. J. Schrader, C. R. Sampson, and T. L. Tsui, 1990: The automated tropical cyclone forecasting system (atcf). *Weather and forecasting*, **5 (4)**, 653–660.

Morgan, M. C., 1999: Using piecewise potential vorticity inversion to diagnose frontogenesis. part i: A partitioning of the q vector applied to diagnosing surface frontogenesis and vertical motion. *Monthly Weather Review*, **127 (12)**, 2796 – 2821, doi: https://doi.org/10.1175/1520-0493(1999)127<2796:UPPVIT>2.0.CO;2, URL https://journals.ametsoc.org/view/journals/mwre/127/12/1520-0493_1999_127_2796_uppvit_2.0.co_2.xml.

NCEP, 2016: List of gfs implementations - 3526 – gfs v14.0.0. URL https://www.emc.ncep.noaa.gov/emc/pages/numerical_forecast_systems/gfs/implementations.php.

Pasch, R. J., A. B. Penny, and R. Berg, 2023: National hurricane center tropical cyclone report hurricane maria. 48, URL https://www.nhc.noaa.gov/data/tcr/AL152017_Maria.pdf.

Rappaport, E. N. and B. W. Blanchard, 2016: Fatalities in the united states indirectly associated with atlantic tropical cyclones. *Bulletin of the American Meteorological Society*, **97 (7)**, 1139 – 1148, doi: https://doi.org/10.1175/BAMS-D-15-00042.1, URL https://journals.ametsoc.org/view/journals/bams/97/7/bams-d-15-00042.1.xml.

Rappaport, E. N., et al., 2009: Advances and challenges at the national hurricane center. *Weather and Forecasting*, **24 (2)**, 395 – 419, doi: https://doi.org/10.1175/2008WAF2222128.1, URL https://journals.ametsoc.org/view/journals/wefo/24/2/2008waf2222128_1.xml.

Rossby, C.-G., 1940: Planetary flow pattern in the atmosphere. quart. *J. Roy. Meteor. Soc.*, **66**, 68–87.

Sampson, C. R. and A. J. Schrader, 2000: The automated tropical cyclone forecasting system (version 3.2). *Bulletin of the American Meteorological Society*, **81 (6)**, 1231–1240.

Schlemmer, L., O. Martius, M. Sprenger, C. Schwierz, and A. Twitchett, 2010: Disentangling the forcing mechanisms of a heavy precipitation event along the alpine south side using potential vorticity inversion. *Monthly Weather Review*, **138 (6)**, 2336 – 2353, doi: https://doi.org/10.1175/2009MWR3202.1, URL https://journals.ametsoc.org/view/journals/mwre/138/6/2009mwr3202.1.xml.

Shapiro, L. J., 1996: The motion of hurricane gloria: A potential vorticity diagnosis. *Monthly Weather Review*, **124 (11)**, 2497 – 2508, doi: https://doi.org/10.1175/1520-0493(1996)124<2497:TMOHGA>2.0.CO;2, URL https://journals.ametsoc.org/view/journals/mwre/124/11/1520-0493_1996_124_2497_tmohga_2_0_co_2.xml.

Simpson, R. H., 1974: The hurricane disaster—potential scale. *Weatherwise*, **27 (4)**, 169–186, doi: 10.1080/00431672.1974.9931702, URL https://doi.org/10.1080/00431672.1974.9931702, https://doi.org/10.1080/00431672.1974.9931702.

Wang, C.-C., K.-Y. Lin, C. A. Davis, S.-Y. Huang, S. C.-S. Liu, K. Tsuboki, and B. J.-D. Jou, 2020: A modeling study on the impacts of typhoon morakot's (2009) vortex structure on rainfall in taiwan using piecewise potential vorticity inversion. *Journal of the Meteorological Society of Japan. Ser. II*, **98 (4)**, 707–733.

Weinkle, J., C. Landsea, D. Collins, R. Musulin, R. P. Crompton, P. J. Klotzbach, and R. Pielke Jr, 2018: Normalized hurricane damage in the continental united states 1900–2017. *Nature Sustainability*, **1 (12)**, 808–813.

Winters, A. C., D. Keyser, and L. F. Bosart, 2020: Composite vertical-motion patterns near north american polar–subtropical jet superposition events. *Monthly Weather Review*, **148 (11)**, 4565 – 4585, doi: https://doi.org/10.1175/MWR-D-20-0140.1, URL https://journals.ametsoc.org/view/journals/mwre/148/11/MWR-D-20-0140.1.xml.

Winters, A. C. and J. E. Martin, 2017: Diagnosis of a north american polar–subtropical jet superposition employing piecewise potential vorticity inversion. *Monthly Weather Review*, **145 (5)**, 1853 – 1873, doi: https://doi.org/10.1175/MWR-D-16-0262.1, URL https://journals.ametsoc.org/view/journals/mwre/145/5/mwr-d-16-0262.1.xml.

Wu, C.-C., S.-G. Chen, C.-C. Yang, P.-H. Lin, and S. D. Aberson, 2012: Potential vorticity diagnosis of the factors affecting the track of typhoon sinlaku (2008) and the impact from dropwindsonde data during t-parc. *Monthly Weather Review*, **140 (8)**, 2670 – 2688, doi: https://doi.org/10.1175/MWR-D-11-00229.1, URL https://journals.ametsoc.org/view/journals/mwre/140/8/mwr-d-11-00229.1.xml.

Wu, C.-C. and K. A. Emanuel, 1995a: Potential vorticity diagnostics of hurricane movement. part 1: A case study of hurricane bob (1991). *Monthly Weather Review*, **123 (1)**, 69 – 92, doi: https://doi.org/10.1175/1520-0493(1995)123<0069:PVDOHM>2.0.CO;2, URL https://journals.ametsoc.org/view/journals/mwre/123/1/1520-0493_1995_123_0069_pvdohm_2_0_co_2.xml.

Wu, C.-C. and K. A. Emanuel, 1995b: Potential vorticity diagnostics of hurricane movement. part ii: Tropical storm ana (1991) and hurricane andrew (1992). *Monthly Weather Review*, **123 (1)**, 93 – 109, doi: https://doi.org/10.1175/1520-0493(1995)123<0093:PVDOHM>2.0.CO;2, URL https://journals.ametsoc.org/view/journals/mwre/123/1/1520-0493_1995_123_0093_pvdohm_2_0_co_2.xml.

Wu, C.-C., T.-S. Huang, and K.-H. Chou, 2004: Potential vorticity diagnosis of the key factors affecting the motion of typhoon sinlaku (2002). *Monthly Weather Review*, **132 (8)**, 2084 – 2093, doi: https://doi.org/10.1175/1520-0493(2004)132<2084:PVDOTK>2.0.CO;2, URL https://journals.ametsoc.org/view/journals/mwre/132/8/1520-0493_2004_132_2084_pvdotk_2.0.co_2.xml.

Wu, C.-C., T.-S. Huang, W.-P. Huang, and K.-H. Chou, 2003: A new look at the binary interaction: Potential vorticity diagnosis of the unusual southward movement of tropical storm bopha (2000) and its interaction with supertyphoon saomai (2000). *Monthly Weather Review*, **131 (7)**, 1289 – 1300, doi: https://doi.org/10.1175/1520-0493(2003)131<1289:ANLATB>2.0.CO;2, URL https://journals.ametsoc.org/view/journals/mwre/131/7/1520-0493_2003_131_1289_anlatb_2.0.co_2.xml.

Wu, C.-C. and Y. Kurihara, 1996: A numerical study of the feedback mechanisms of hurricane–environment interaction on hurricane movement from the potential vorticity perspective. *Journal of Atmospheric Sciences*, **53 (15)**, 2264 – 2282, doi: https://doi.org/10.1175/1520-0469(1996)053<2264:ANSOTF>2.0.CO;2, URL https://journals.ametsoc.org/view/journals/atsc/53/15/1520-0469_1996_053_2264_ansotf_2_0_co_2.xml.

APPENDIX

THE PIECEWISE POTENTIAL VORTICITY INVERSION TOOL

The piecewise potential vorticity (PV) inversion tool inverts PV perturbations to retrieve the balanced fields from individual PV perturbations. This tool ingests global fields of temperature, geopotential height, and temperature and calculates Ertel PV. PV pertaining to the hurricane circulation (i.e., basic PV) is separated from the total PV field, which isolates the PV around the hurricane environment (i.e., perturbation PV). The PV perturbation field is partitioned using the scheme described in the methodology section. The total PV perturbation field and each piece of PV perturbation is inverted to retrieve the balanced fields pertaining to the PV that is inverted. The balanced fields describe how each PV perturbation influences the atmosphere in the form of a non-divergent wind field and pressure field. The mathematical framework to perform these inversions uses a nonlinear balanced relation to invert Ertel PV. This package is composed of several scripts written mainly in Fortran 90 and Python, and is wrapped in C-Shell scripts. The filepaths, environmental variables and namelist variables can be changed in the C-shell wrapper scripts to adapt to the user's needs. The piecewise PV inversion tool is publicly available on Github: https://github.com/tbarbero/PPVI.

The first script in the chain is called *run_pv1.csh* which executes *pv1.F90*. Global h,t,u and v are ingested at 1^o horizontal grid resolution,

- Input Files
  - Global 1^o by 1^o h, t, u, v
- Output Files
  - yyyymmdd_hhZ_htuv.nc
  - yyyymmdd_hhZ_pv.nc
- Objective
  (1) A subset of the region is cut out based on namelist parameters: 'west', 'east', 'north', and 'south'.
  (2) A 9-point local smoothing function is applied on the new domain.
  (3) Write out smoothed, regional h,t,u,v in a .nc file
  (4) Adjust h ensuring that static stability is positive everywhere ($dh/dp > 0$). This is a condition to solve the elliptical partial differential equation to get Φ and Ψ
  (5) Compute relative vorticity from u and v, and then compute the streamfunction Ψ from relative vorticity
  (6) Compute Ertel PV
  (7) Compute the non-divergent wind from the stream function
  (8) Write out calculated PV, adjusted h, Ψ, non-divergent u, v, absolute vorticity

The second script *find_TC_center.py* takes in the best track position and calculated PV, and computes the location of the hurricane center based on the grid location of the vertically averaged maximum positive PV value.

- Input Files
  - 2017.NAtl.stormnum.txt
  - yyyymmdd_hhZ_pv.nc
- Output Files
  - center.txt
- Objective

(1) For all initialized runs of a storm, compute the TC storm center out to 240Z every 6 hours
(2) Load in regional PV file, vertically average PV from 925 to 300hPa [forecast_times,lat,lon]
(3) Grab initial TC storm center guess (lat.xx, lon.xx) and make a 5^o x 5^o box around center on PV data
(4) Perform a rectangular bivariate spline interpolation for PV box for a more accurate center
(5) Find location of maximum positive PV value
(6) Write out 6-hr hurricane center forecast out to 240Z for each initialized run in *center.txt*

The third script *run_symhtuv.csh* runs *symhtuv1.F90*.

- Input Files
  - yyyymmdd_hhZ_htuv.nc
  - yyyymmdd_hhZ_pv.nc
  - center.txt
- Output Files
  - yyyymmdd_hhZ_htuv2.nc
  - yyyymmdd_hhZ_symhtuv.nc
- Objective
  (1) Load in adjusted height and Ψ from *yyyymmdd_hhZ_pv.nc* and temperature from *yyyymmdd_hhZ_htuv.nc*
  (2) Compute basic fields: height, stream function, and temperature by taking the axisymmetric in a 2000km radius from hurricane center
  (3) Compute perturbation fields by subtracting basic fields from the total fields
  (4) Compute basic and perturbation non-divergent winds from associated stream functions, individually

The fourth script is *run_pv2.csh* which runs *pv2.F90*.

- Input Files
  - yyyymmdd_hhZ_htuv2.nc
- Output Files
  - yyyymmdd_hhZ_pv2.nc (Total fields)
- Objective
  (1) Repeat computing parts in *pv1.F90*, but use the non-divergent winds

The fifth script is *run_pvb.csh* which runs *pvb.F90*.

- Input Files
  - yyyymmdd_hhZ_symhtuv.nc
- Output Files
  - yyyymmdd_hhZ_pvb.nc
- Objective
  (1) Repeat computing parts in *pv1.F90* but use the basic fields

The sixth script is *run_sqinvph.csh* which runs *sqinvph.F90*

- Input Files
  - yyyymmdd_hhZ_pvb.nc
  - yyyymmdd_hhZ_pv2.nc
- Output Files
  - yyyymmdd_hhZ_sqinvph.nc
- Objective
  (1) Compute perturbation field by subtracting basic fields from total field
  (2) Compute the non-divergent wind associated with the total PV perturbation

The seventh script is *mask_region.py*.

- Input Files
  - yyyymmdd_hhZ_sqinvph.nc
- Output Files
  - Binary flat masked PV regions (i.e., *system.1*, system.2, ..., *system.40*)
- Objective
  (1) Read in total PV perturbation field and TC center location
  (2) Cut up the total PV perturbation field into different regions
  (3) Cut the negative PV perturbation into static Bermuda High (BH) and Continental High (CH)
  (4) Cut the positive PV pertubation into four ordinal (NW,NE,SE,SW) qudrants relative to the storm center at each forecast time
  (5) Save the cut PV perturbation for each region for each forecast time as a binary flat file

The eighth script is called *run_sqinvmask.csh*.

- Input Files
  - yyyymmdd_hhZ_pvb.nc
  - yyyyyyymmdd_hhZ_pv2.nc
  - all mask files for one system (i.e., *system.1*, system.2, ..., *system.40*)
- Output Files
  - yyyymmdd_hhZ_system.nc
- Objective
  (1) Read in total PV perturbation field and TC center location
  (2) Cut up the total PV perturbation field into different regions
  (3) Cut the negative PV perturbation into static Bermuda High (BH) and Continental High (CH)
  (4) Cut the positive PV pertubation into four ordinal (NW,NE,SE,SW) qudrants relative to the storm center at each forecast time
  (5) Save the cut PV perturbation for each region for each forecast time as a binary flat file

The ninth script is called *run_steersq.csh*.

- Input Files

  - yyyymmdd_hhZ_sqinvph.nc (u, v associated with total pv perturbation) or
  - yyyymmdd_hhZ_system.nc (u, v associate with pv perturbations of particular system)
- Output Files
  - yyyymmdd_hhZ_steering_3degree_system
- Objective

  (1) Calculate the average u-,v-wind in a circle of 3^o radius around the TC center for each level at each forecast time. The radius within which values are averaged can be changed in the *steersq.nml* file.